Minimum Loss Operation and Optimal Design of High-Frequency Inductors for Defined Core and Litz Wire

PANTELEIMON PAPAMANOLIS (Student Member, IEEE), **THOMAS GUILLOD** (Member, IEEE),
FLORIAN KRISMER (Member, IEEE), AND **JOHANN W. KOLAR** (Fellow, IEEE)

Power Electronic Systems Laboratory (PES) ETH Zurich, ETH Zurich Physikstrasse 3, 8092 Zurich, Switzerland

CORRESPONDING AUTHOR: PANTELEIMON PAPAMANOLIS (e-mail: papamanolis@lem.ee.ethz.ch)

ABSTRACT This paper studies the loss-optimal design of a power inductor employed in a 2 kW, 400 V input DC–DC converter. The design of an inductor is subject to a large number of design parameters and the implications of the different design parameters on the losses are often not clearly traceable in a full optimization, e.g., different current ripple amplitudes can lead to designs with similar losses, as larger ripple amplitudes lead to increased AC core and winding losses but lower DC losses in the winding due to lower inductance values and/or numbers of turns. In an effort to achieve a comprehensible description of the implications of the key design parameters (switching frequency, f_s, current ripple, r, number of turns, N) on the losses, the remaining parameters, e.g., core (E55/28/21 N87) and type of conductor (litz wire), are considered to be given. In a first step, the investigation is based on a simplified analytical model, which is refined in a step-by-step manner, e.g., to consider core saturation. In a second step, the implications of further critical aspects on the losses, e.g., temperatures of core and coil, are examined using a comprehensive semi-numerical model. Surprisingly, the evaluation of the losses calculated in the f_s–r domain reveals that nearly minimum inductor losses are obtained for a current ripple that is inversely proportional to the frequency, i.e., for a constant inductance, within a wide frequency range, from 200 kHz to 1 MHz. Furthermore, the investigation reveals a decrease of the losses for increasing frequencies up to 375 kHz, e.g., from 4.32 W at 80 kHz ($r = 110$ %) to 2.37 W at 375 kHz ($r = 18$ %). The detailed analysis related to these results enables the compilation of a simple two-equation guide for the design of an inductor that achieves close to minimum losses. In a next step, interesting trade-offs are identified based on a study of the design space diversity, e.g., with respect to low cost and increased partial-load efficiency. The findings of this work are experimentally verified, i.e., the losses of three different inductors are measured with an accurate calorimetric method and at four different frequencies, ranging from 150 kHz to 700 kHz.

INDEX TERMS Inductor optimization, analytical model, calorimetric measurement, core losses, design space diversity, ferrite, litz wire, minimum losses, performance factor, semi-numerical model, system design.

I. INTRODUCTION

Wide-bandgap semiconductors have lead to unprecedented switching frequencies, f_s, for power converters up to several MHz, commonly using modulation strategies that allow for soft transitions of the semiconductors (e.g., Triangular Current Modulation, TCM) [1], [2]. This is motivated by the expected increase in the power density on the system level, mainly due to the decrease of the volume of the magnetic components

and/or the filtering requirements, e.g., with respect to the EMI CISPR regulations. Literature confirms this trend [3], nevertheless, only from a system-level perspective. Applicability of this expectation on the magnetic components directly is not evident, and common misconceptions, according to which magnetic components represent the bottleneck of the complete systems, or that increasing frequency always leads to smaller components, and/or that 50% of allowed relative

peak-to-peak current ripple, r, is approximately optimal, remain unanswered. Investigations on a system level are less suitable to clarify the above, since designs with significantly different design parameters can map to nearly same overall performance values (e.g., efficiency, power density). This effect arises from different trade-offs and is referred to as design space diversity [1]; by way of example, increased switching frequencies may lead to smaller magnetic components but larger cooling systems, due to increased switching losses. Hence, individual component investigations are mandatory.

Such type of analysis has been previously conducted in literature, but mostly with respect to the operation of medium-frequency transformers. Specifically, using the Performance Factor ($PF = B_{tot}f_s$), the optimal region of operation of a transformer, with respect to the applied level and frequency of the magnetic flux density is defined [4]–[7]. This is further improved in [8], where the impact of the High-Frequency (HF) copper losses is also considered. A more systematic and detailed approach is presented in [9], [10]. However, these considerations are not directly applicable to inductors, since critical key design parameters differ. Specifically, inductor designs feature an additional Low-Frequency (LF) core premagnetization component and also a different distribution of the magnetic field inside the winding window, due to the fringing-field caused by the air gap. The value of the inductance components of an inductor related to the stray field and the field in the magnetic core is more critical compared to transformers and, depending on the choice of f_s and L, the RMS value of the AC current component varies, whereas in the case of the transformer it remains constant. Therefore, individual analysis of power inductors is required.

Multiple references exist in literature solely focusing on inductor optimization, divided into simple analytical models [11]–[14], semi-numerical and data-based models [15], the most recent convex optimization geometric program formulation [16] and finite elements optimization [17], [18]. Nevertheless, all the above focus on the modeling and optimization procedures and not on understanding the actual optimal operation of power inductors, which serves the main motivation behind this paper. Such knowledge is critical for the evaluation of the validity of different optimization results, and also for the parametrization of the optimization algorithms, in order to become more computationally efficient, by accurately focusing on the main objectives and the investigated range of the design space [19].

As the following considerations should allow to gain insight into key parameter dependencies, the number of parameters that take influence on the inductor losses are reduced to a minimum, cf. Fig. 1. Specifically, the magnetic core (N87 TDK - E55/28/21) and the type of conductor (litz wire with single strand diameter, d_r, of 100 μm) are assumed as given. Moreover, the simple topology of a 2 kW DC–DC buck converter, cf. Fig. 2(a) is considered, that is operated with constant input and output voltages, and a sinusoidal instead of a triangular shape of the AC current ripple, with the same peak value,
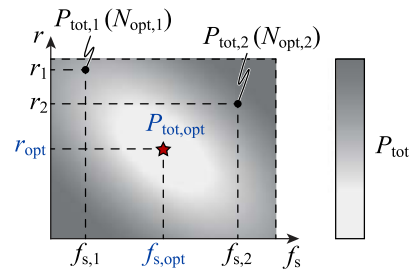
System parameter (for provided specifications)

• **Switching frequency** - f_s

Inductor design parameters

• **Current ripple** - r

• **Number of turns** - N
• **Air-gap length**
  } **Modified for each pair of (f_s, r)**
  Condition: achieve r for given f_s
  Goal: minimize total losses - P_{tot}

• **Core geometry:** shape, volume, aspect ratios, single/distributed gap
• **Core material:** MnZn ferrite, NiZn ferrite etc.
• **Coil type:** solid wire, litz wire (diff. strand diam.), foil, flat wire, conventional/optimized turn place.
• **Coil material:** copper, aluminum etc.
  } **Considered fixed**

FIGURE 1. Compilation of typical degrees of freedom available in an inductor design. This work focuses on the choice of two key parameters, namely, switching frequency and current ripple, while ensuring an optimal choice of the number of turns and the air gap length. Further design parameters, e.g., magnetic core and type of conductor, are considered given.
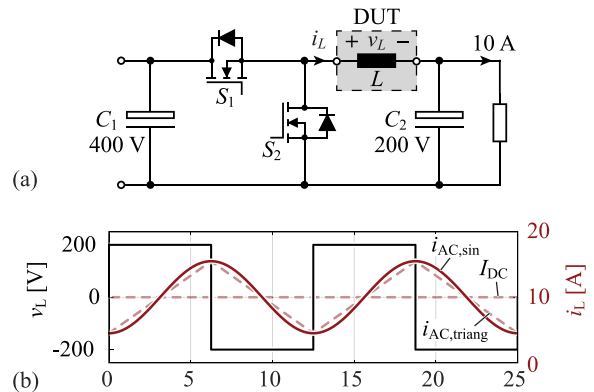

FIGURE 2. (a) Considered topology of a DC-DC buck converter; (b) example of the considered sinusoidal waveform of the current ripple instead of a triangular shape, for f_s = 80 kHz switching frequency and r = 110% relative peak-to-peak current ripple.

is assumed (cf. Fig. 2(b)), which typically results in a slight overestimation of the core losses [20].

Moreover, the above considerations do not have an impact on the generality of the findings, since similar magnetic excitations apply to typical AC–DC and DC–AC topologies, i.e., triangular voltage-imposed flux density waveform, LF current-imposed premagnetization. The implications of different core shapes on the core losses can be considered by

a constant shape factor [21]. Finally, different ferrite materials exhibit similar loss characteristics, in different frequency ranges, as shown in the performance factor graphs presented in [22], [23].

With this, the paper can emphasize on the implications of the remaining three design degrees of freedom, i.e.,

1) switching frequency, f_s
2) relative peak-to-peak current ripple (or inductance),

$$r = \frac{2I_{AC,pk}}{I_{DC}} \text{ with } I_{AC,pk} = \frac{V_o}{4f_sL}, \quad (1)$$

3) number of turns, N,

on the losses. In Section II, the impact of critical non-linearities, i.e., saturation of the magnetic core and varying Steinmetz parameters for different magnetic flux waveform characteristics (e.g., frequency, amplitude), is investigated using simple analytical equations. In addition, the optimal $f_s - r$ operating area with regard to minimal inductor losses is inspected in detail, revealing a flat characteristic around the minimum. In a second step, Section III proposes and evaluates a detailed semi-numerical model in order to take the following aspects, which have been omitted in Section II, into account.

- More accurate calculation of the copper AC resistance (e.g., by detailed calculation of the magnetic field in the core window);
- Impacts of f_s, AC and DC flux densities, and core temperature on the core losses;
- Detailed thermal model;
- Placement of each turn in the coil (turn packaging).

Based on this, the initial findings from the analytical models are confirmed. The results presented in Section III, which are obtained for given core and single strand diameter, denote the basis for further evaluation in Section IV, where different design considerations are analyzed, i.e., distributed air gap, different strand diameter of the litz wire, and different core size. Section V presents a simple "two-equations" guide that directly leads to quasi-optimal designs, and in Section VI the design space diversity of inductors is investigated, which reveals potentially missed design opportunities, with respect to quasi-optimal designs (i.e., up to +20% losses from the global optima $P_{gl,opt}$, but at lower manufacturing cost and improved partial load efficiency) [1], [9]. Finally, in Section VII, all the above-mentioned findings are further confirmed through experimental verification.

II. ANALYTICAL MODEL AND BASIC DESIGN PRINCIPLES

Table 1 lists the specifications of the considered DC–DC buck converter, which have their origin in typical specifications of commercial solar inverters; the output to input voltage ratio of 0.5 has been selected in order to consider maximum current ripple. The considered ambient temperature, T_{amb}, at 60 °C corresponds to a commonly considered maximum case temperature of a converter [24]. In addition, in Table 2, the main geometrical and electrical parameters of the considered inductor are presented. The N87 ferrite core material of TDK-EPCOS is a commonly used low-cost material that features

TABLE 1. Main Specification

Parameter	Value
Topology	DC-DC buck converter
Nominal power (P_{nom})	2 kW
Input voltage (V_i)	400 V
Output voltage (V_o)	200 V
Considered frequencies (f_s)	[40, 1000] kHz
Efficiency profile	Euro weighted efficiency [26]
Ambient temperature (T_{amb})	60 °C
Cooling mechanism	Natural convection

TABLE 2. Main Design Parameters

Parameter	Value
Ferrite core	MnZn N87 E 55/28/21
Type of coil	Round litz wire, $d_r = 100\,\mu m$
Core volume (V_C)	44000 mm³
Core cross-section (A_C)	353 mm²
Winding window area (A_W)	250 mm²
Winding window width (w_W)	10.2 mm
Average turn length (l_{avg}) [1]	116 mm
Copper fill factor (k_f) [1]	30 %
Copper conductivity (σ) [1]	$50 \cdot 10^6$ S/m
Mag. flux density sat. (B_{sat})	360 mT
Steinmetz par. (k_{SE}, α, β) [1]	9.66, 1.30, 2.59
Core temperature (T_{core}) [1]	80 °C

[1]This value applies only to the analytical model, discussed in Section II.

minimum losses for core temperatures between 80 °C and 90 °C and achieves a high performance factor [22] in the considered operating range. The chosen E55/28/21 core allows for a thermally valid operation in an wide range of f_s and r. For this model, a distributed air gap on the centered limb is considered, since, for this special case, an analytical solution exists for the magnetic field distribution inside the core window [25]. Finally, the selected litz wire with a single strand diameter of $d_r = 100\,\mu m$ is a good compromise between low losses and cost in the investigated ranges of f_s and r.

A. NONSATURABLE CORE, CONSTANT STEINMETZ PARAMETERS

In a first step, the analysis neglects the presence of magnetic flux density saturation, the frequency and flux density dependence of the Steinmetz parameters, and the influence of the core DC premagnetization on the core losses. Even though this approach is of limited accuracy, its results enable the deduction of first conclusions with regard to suitable values of f_s, r, and N.

The inductor losses are split into copper and core losses. The copper losses feature DC and AC components,

$$P_{Cu,tot} = \underbrace{R_{DC}I_{DC}^2}_{P_{Cu,DC}} + \underbrace{c_0 R_{DC}\frac{I_{AC,pk}^2}{2}}_{P_{Cu,AC}}, R_{DC} = \frac{Nl_{avg}}{\sigma k_f \frac{A_W}{N}}, \quad (2)$$

where c_0 considers skin and proximity effects [25],

$$c_0 = \begin{cases} 1 + \frac{1}{12}\left(\frac{k_f w_w d_r}{\delta^2}\right)^2 & \forall\, d_r < 3.17\delta, \\ \frac{1}{\delta}\left(\frac{d_r}{4} + \frac{8(k_f w_w)^2}{3 d_r}\right) & \forall\, d_r \ge 3.17\delta. \end{cases} \quad (3)$$

In (3), δ and w_w denote the skin depth and the width of the core window, respectively.

The magnetic flux density can be separated into a current-imposed DC component and a voltage-imposed AC component,

$$B_{DC} = \frac{L I_{DC}}{N A_c}, \qquad B_{AC} = \frac{V_o}{4 f_s N A_c}. \quad (4)$$

Since the implications of B_{DC} on the core losses are neglected in this Section, only B_{AC} contributes to the core losses, which, for sinusoidal waveforms, are calculated with the Steinmetz Equation (SE) [27],

$$P_{core} = V_c k_{SE} f_s^\alpha B_{AC}^\beta = V_c k_{SE} f_s^{\alpha-\beta}\left(\frac{V_o}{4 N A_c}\right)^\beta. \quad (5)$$

With (2) and (5) the total inductor losses are

$$P_{tot} = P_{Cu,tot} + P_{core} = c_1 N^2 + c_2 N^{-\beta} \quad (6)$$

with

$$c_1 = \frac{P_{Cu,tot}}{N^2} = \frac{(32 f_s^2 I_{DC}^2 L^2 + c_0 V_o^2)\, l_{avg}}{32 \sigma A_w k_f f_s^2 L^2}, \quad (7)$$

$$c_2 = \frac{P_{core}}{N^{-\beta}} = V_c f_s^{\alpha-\beta} k_{SE}\left(\frac{V_o}{4 A_c}\right)^\beta. \quad (8)$$

For $dP_{tot}/dN = 0$, the optimal number of turns,

$$N_{opt} = \left(\frac{\beta}{2}\frac{c_2}{c_1}\right)^{\frac{1}{2+\beta}}, \quad (9)$$

results, which enables the derivation of the optimum ratio between core and copper losses, with respect to minimum total losses, as often stated in literature [28], [29],

$$\left.\frac{P_{core}}{P_{Cu,tot}}\right|_{N=N_{opt}} = \frac{2}{\beta}. \quad (10)$$

The minimum total losses for given inductance and switching frequency are

$$P_{tot,opt} = P_{tot}(N_{opt}) = c_3\left(\frac{c_4 f_s^2 L^2 + 1}{L^2}\right)^{\frac{\beta}{2+\beta}} f_s^{\frac{2(\alpha-2\beta)}{2+\beta}}, \quad (11)$$

with

$$c_3 = (2+\beta)\left[\left(\frac{k_{SE} V_o^{2\beta} V_c}{2 A_c^\beta}\right)^2\left(\frac{c_0 l_{avg}}{512 A_w k_f \sigma \beta}\right)^\beta\right]^{\frac{1}{2+\beta}}, \quad (12)$$

$$c_4 = \frac{32 I_{DC}^2}{c_0 V_o^2}. \quad (13)$$

According to (11) and for constant frequency, the total losses for $N = N_{opt}$ monotonically decrease for increasing inductance and, for $L \to \infty$,[2] converge to

$$P_{tot,opt}(f_s)\big|_{L\to\infty} = P_{conv}(f_s) = c_3 c_4^{\frac{\beta}{2+\beta}} f_s^{\frac{2(\alpha-\beta)}{2+\beta}}. \quad (14)$$

The resulting non-zero value of $P_{conv}(f_s)$ is related to the fact that both, copper losses and core losses, cannot approach zero, since I_{DC} and B_{AC} are constant (independent of L - assuming constant N) and greater than zero. In addition, the copper losses increase for increasing N and the core losses decrease for increasing N, cf. (2) and (5). Thus, for $L \to \infty$, the optimal number of turns converges to a finite value greater than zero, too, in order to maintain $P_{core}/P_{Cu,tot} = 2/\beta \approx P_{core}/P_{Cu,DC}$,

$$\lim_{L\to\infty} N_{opt} = N_{conv} = c_5 f_s^{\frac{\alpha-\beta}{2+\beta}}, \quad (15)$$

$$c_5 = \left(\frac{2^{-1-2\beta}\sigma A_w k_f k_{SE}\beta\left(\frac{V_o}{A_c}\right)^\beta V_c}{I_{DC}^2 l_{avg}}\right)^{\frac{1}{2+\beta}}. \quad (16)$$

In contrast, the value of $P_{conv}(f_s)$ monotonically decreases for increasing frequency, given that $\alpha < \beta$ applies, and converges to zero for $f_s \to \infty$, cf. (14). The reason for this result can be explained based on the decrease of the voltage time area due to the increase of f_s, which enables a decrease of the core losses. This, in turn, is accompanied by a decrease of the copper losses in order to maintain $P_{core}/P_{Cu,tot} = 2/\beta$. Accordingly, also N_{opt} approaches zero for $f_s \to \infty$ (to approach zero copper losses).[3]

Fig. 3(a) depicts an f_s–r contour plot of the total losses (including losses due to skin and proximity effects) for the parameters listed in Tab. 2 and an extended range of operating points, i.e.,

$$50\text{ kHz} \le f_s \le 1\text{ MHz and } 1\% \le r \le 500\%, \quad (17)$$

to obtain a more complete picture.[4] Fig. 3(a) confirms the findings described above:

1) For a given frequency, minimum total losses result for $L \to \infty$ (corresponding to $r \to 0$);
2) The value of $P_{conv}(f_s)$, i.e., the total losses for $r \to 0$, decreases for increasing frequency.

B. SATURABLE CORE, CONSTANT STEINMETZ PARAMETERS

For L approaching infinity and N approaching the finite value N_{conv}, the current-imposed DC flux component approaches infinity, cf. (4). This is not realistic, due to saturation of the magnetic core. In the following, the magnetic flux density

---

[2]$L \to \infty$ is theoretically evaluated by assuming infinite permeability of the ferrite core and an air gap that approaches zero.

[3]For the analysis, a non-integer number of turns is allowed.

[4]The maximum ripple in a practical system with MOSFET semiconductors may not exceed the value needed for quasi-lossless switching, i.e., approximately 200%.
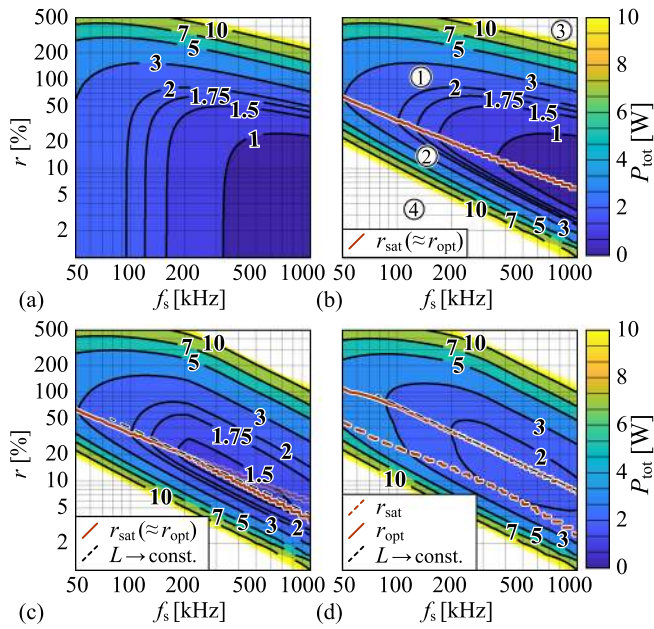
FIGURE 3. Contour plots of the total losses, for the f_s–r-plane defined with (17) and four distinct cases: (a) no saturation limit, constant Steinmetz parameters; (b) saturation limit of 360 mT, constant Steinmetz parameters; (c) and (d) saturation limit of 360 mT, operating-point dependent Steinmetz parameters; (c) only considers the implications of B_{AC} and f_s on k_{SE}, α, and β; (d), in addition, takes the impact of B_{DC} on the Steinmetz parameters into account.
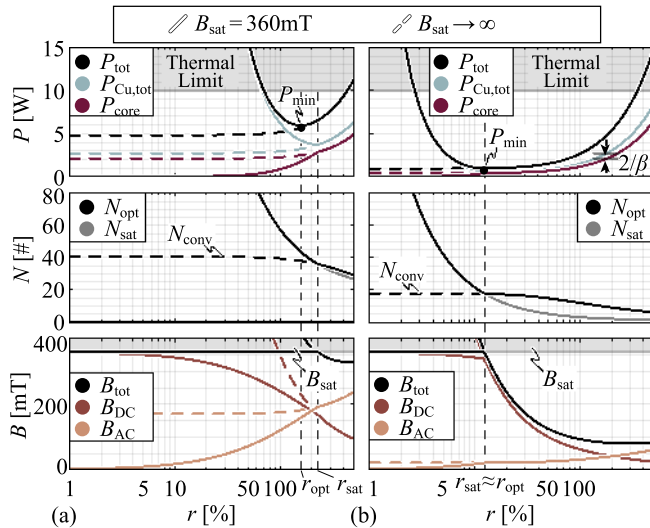

FIGURE 4. Investigation of the optimal ripple (or inductance), r_{opt} (or L_{opt}), for two different frequencies, i.e., (a) 20 kHz, and (b) 375 kHz. For both frequencies, the cases of magnetic flux density going to infinity and limited at 360 mT are depicted.

saturation limit of the considered ferrite core, B_{sat}, is set to 360 mT.

In order to get an understanding of the implications of the magnetic flux density saturation limit on the optimal ripple value, Fig. 4 presents the characteristics of the losses, the optimal number of turns for given r and f_s, and the flux densities with respect to ripple and for two different frequencies

of 20 kHz and 375 kHz.[5] It can be observed that, due to $B_{DC} + B_{AC} \leq B_{sat}$, a clear loss minimum, P_{min}, results for a given frequency, which appears at a ripple r_{opt} that is slightly less but close to r_{sat}, i.e., the ripple where the theoretically calculated magnetic flux density is equal to the saturation magnetic flux density. Below this ripple there is a steep increase of N, in order to limit the magnetic flux density. The difference between r_{opt} and r_{sat} arises, because in this limited interval the decrease of the AC copper losses, $P_{Cu,AC}$, for decreasing r, together with the decrease of P_{core} due to the increase of N, outweigh the increase of the DC resistance, R_{DC}. A theoretical verification of the impact of $P_{Cu,AC}$ on r_{opt} has been conducted by applying $P_{Cu,AC} = 0$ in (2), which yields

$$P_{tot} = P_{min} \ \forall \ r \geq r_{sat} \quad \Leftrightarrow \quad P_{Cu,AC} = 0. \quad (18)$$

Even though this result is mainly of theoretical value, it confirms that $r_{opt} < r_{sat}$ can only result for $P_{Cu,AC} > 0.$,[6] With increasing frequency, the values of r_{sat} and r_{opt} decrease and, in addition, r_{opt} approaches r_{sat}, e.g., at 375 kHz, $r_{opt} \approx r_{sat}$ applies.

The f_s–r contour plot of the total losses that considers the saturation limit is shown in Fig. 3(b). Four regions are highlighted. Region ① corresponds to thermally valid designs that are not limited by saturation and can acquire their corresponding optimal number of turns. Region ② corresponds to designs that are limited by saturation. The trajectory of r_{sat}, which is approximately equal to the trajectory of r_{opt}, delimits the two regions. Regions ③, ④ correspond to thermally invalid designs due to excessive AC copper/core losses and DC copper losses, respectively.

No analytical solution has been found for r_{opt}, however, an analytical expression can be derived for r_{sat} and, using (1), for L_{sat}. Subsequently, $L_{opt} \approx L_{sat}$ is considered, based on the assumption that r_{opt} is close to r_{sat}. Starting with (4),

$$B_{tot} = B_{DC} + B_{AC} = B_{sat} \Rightarrow N = \frac{4f_s L I_{DC} + V_o}{4f_s A_c B_{sat}} \quad (19)$$

applies for N. Furthermore, N needs to be equal to N_{opt}, cf. (9), in order to obtain minimum losses. The equation $N = N_{opt}$ can be solved with respect to L based on the assumption that $B_{DC}^2 \gg B_{AC}^2$ applies,[7] which is a valid assumption in the

---

[5] The frequency value of 20 kHz is considered only in this section for better understanding of the analysis, nevertheless, it is a non-optimal frequency for the considered core material and, thus, for the rest of the analysis is omitted.

[6] In addition, and in anticipation of the results discussed in Section III the finding (18) will contribute to the reason why the loss optimum computed with the detailed inductor model is rather flat within a relatively wide range of r.

[7] By applying (4) to $B_{DC}^2 \gg B_{AC}^2$, the inequality $16(f_s L I_{DC})^2 \gg V_o^2$ results. With this, and for the assumption of a negligible impact of high-frequency losses due to skin and proximity effects ($c_0 = 1$), the expression $32(f_s L I_{DC})^2 + c_0 V_o^2$, which appears in the course of the derivation of (20), can be replaced by $32(f_s L I_{DC})^2$.
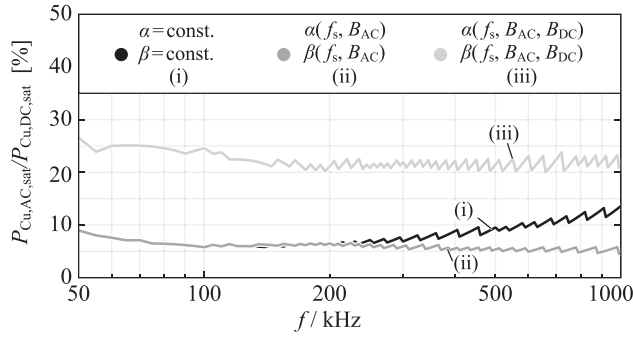
FIGURE 5. Ratio of AC to DC copper losses with respect to switching frequency and for $L = L_{sat} \approx L_{opt}$. The cases with and without consideration of the AC proximity losses are depicted.

considered frequency range. With this,

$$N_{opt} \approx \left(\frac{\sigma A_w k_f k_{SE} \beta \left(\frac{V_o}{A_c} \right)^\beta V_c f_s^{\alpha - \beta}}{2^{1+2\beta} I_{DC}^2 l_{avg}} \right)^{\frac{1}{2+\beta}} \qquad (20)$$

and

$$L_{sat} \approx \underbrace{c_6 f_s^{\frac{\alpha - \beta}{2 + \beta}}}_{L_{sat,a}} - \underbrace{\frac{V_o}{4 f_s I_{DC}}}_{L_{sat,b}} \approx L_{opt}, \qquad (21)$$

$$c_6 = \frac{A_c^{\frac{2}{2+\beta}} B_{sat} \left(2^{-1-2\beta} \sigma A_w k_f k_{SE} \beta V_o^\beta V_c \right)^{\frac{1}{2+\beta}}}{I_{DC}^{\frac{4+\beta}{2+\beta}} l_{avg}^{\frac{1}{2+\beta}}} \qquad (22)$$

result.

Compared to the numerically derived value of L_{sat}, (21) results in a maximum deviation of 0.64% at $f_s = 100$ kHz and converges to zero for increasing frequency. At higher frequencies, the first term, $L_{sat,a}$, becomes dominant and, in a double-logarithmic representation,

$$\log(L_{sat,a}) = \log(c_6) + \frac{\alpha - \beta}{2 + \beta} \log(f_s), \qquad (23)$$

$\log(L_{sat,a})$ is directly proportional to $\log(f_s)$. By way of example, for the settings listed in Table 2 ($\alpha = 1.30$, $\beta = 2.59$), $(\alpha - \beta)/(2 + \beta) = -0.28$ results, which, in terms of decibel, corresponds to a change of $L_{sat,a}(f_s)$ by -5.6 dB/decade.

According to the findings related to (18), $L_{opt} \approx L_{sat}$ is valid if the AC copper losses have a negligible impact on the DC losses, i.e., for a low ratio of AC to DC copper losses. At $L = L_{sat}$, this ratio is obtained based on (2) and (20),

$$\frac{P_{Cu,AC,sat}(f_s)}{P_{Cu,DC,sat}(f_s)} 100\% \approx \frac{c_0}{32} \left(\frac{V_o}{f_s L_{sat} I_{DC}} \right)^2 100\%. \qquad (24)$$

For the considered specifications, the result, marked with (i) in Fig. 5, shows that the AC copper losses are less than 15% of the DC copper losses within the complete range of considered frequencies, and the calculated relative error between P_{min} and $P_{tot}(r_{sat})$ is less than 1%. Nevertheless, even for the extreme case previously considered of 20 kHz evaluation revealed that
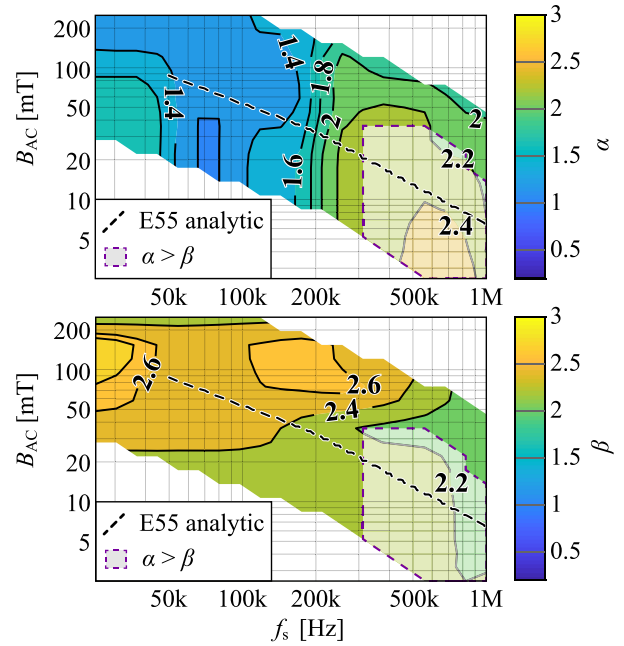

FIGURE 6. Contour plot of the values of the Steinmetz parameters α, β with respect to the amplitude and the frequency of the applied AC magnetic flux density. The values are extracted using local Least Mean Square (LMS) fitting of the Steinmetz Equation on measured loss-data at 80 and a DC premagnetization equal to 0 mT (cf. Section III). Additionally, a trajectory is highlighted that corresponds to the optimal designs, L_{opt}, of E55/28/21 core depicted in Fig. 3(c), Fig. 7.

the relative error between P_{min} and $P_{tot}(r_{sat})$ drops below 8% already for an AC to DC copper ratio equal to 50%.

Finally, since the condition $P_{Cu,AC} \ll P_{Cu,DC}$ at L_{sat} for $f_s \in [50$ kHz, 1000 kHz] is validated, the optimal losses and number of turns, that correspond to each L_{opt} - f_s pair can be directly calculated using (15) and (14), respectively. Comparison between the estimated ones through (15) and (14) and the ones using a brute-force evaluation approach returns an absolute maximum error below 1% that converges towards zero with increasing frequency, for both values.

C. STEINMETZ PARAMETERS DEPENDENT ON f_S AND B_{AC}

Since the Steinmetz parameters are obtained from an exponential fitting to measured core losses of the employed material, they are only valid within a limited range of operation. In order to increase the accuracy of the computed core losses, the employed Steinmetz parameters need to be adapted to the operating point, which, with regard to core losses, is mainly characterized by the magnetic flux density (frequency, amplitude of AC component, DC bias) and the core temperature. Fig. 6(a), **(b)** depicts the values of α and β with respect to f_s and B_{AC} for the N87 material, $T_{core} = 80$ °C, and $B_{DC} = 0$. The values are obtained with local Least Mean Square (LMS) fittings of the Steinmetz Equation (SE) to measured losses (cf. Section III). It can be seen that $\alpha < \beta$ applies for most combinations of f_s and B_{AC}, except for high frequencies, where the two parameters show approximately equal values; for $f > 350$ kHz even $\alpha > \beta$ applies at some
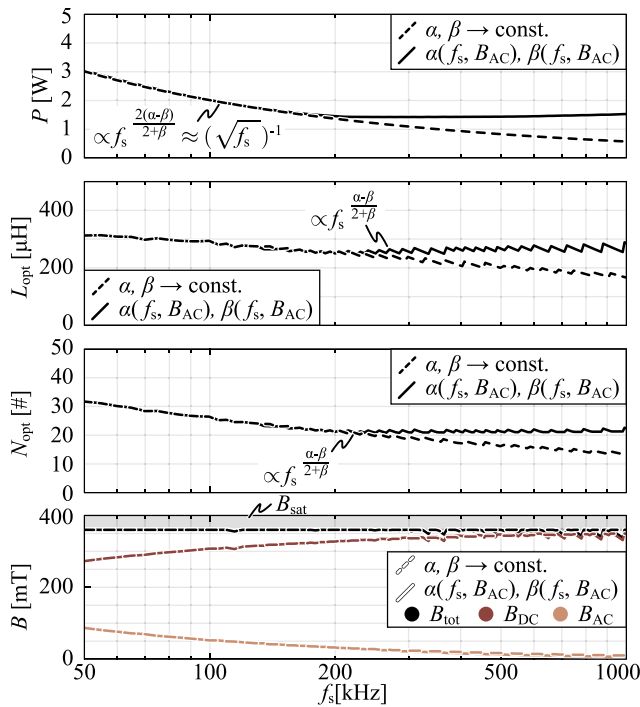
FIGURE 7. Loss-optimal designs over frequency using the analytical model for three distinct cases, i.e., i. no AC proximity losses and constant Steinmetz parameters, ii. with AC proximity losses and constant Steinmetz parameters, iii. with AC proximity losses and Steinmetz parameters that take into consideration the impact of AC magnetic flux density and switching frequency for a constant temperature of 80° C and $B_{DC} = 0$ mT.

FIGURE 8. Comparison of the main performance characteristics of the two trajectories L_{opt} and L_{sat} depicted in Fig. 3(d).

regions. The white regions in Fig. 6 correspond to regions where the resulting loss density is outside the limits of interest, i.e., 0.5 kW/m^3 $< p_{core} < 1000$ kW/m^3. It should be noted that that these two maps change for different values of T_{core} and B_{DC}.

Fig. 3(c) shows a contour plot of the losses that results for (6) if the impact of the frequency and the AC magnetic flux density on the Steinmetz parameters is considered. The contour plot reveals a significantly flat region of low losses between 200 kHz and 1000 kHz. Since the characteristic properties of the losses along the minimum-loss trajectory marked with L_{opt} are of particular interest, Fig. 7 presents a direct comparison of P_{tot}, L, N, B_{DC}, B_{AC}, and B_{tot} along these trajectories in Fig. 3(b) and Fig. 3(c), i.e., for constant and for operating-point dependent Steinmetz parameters (with respect to f_s, B_{AC}). In addition, the minimum-loss trajectory of Fig. 3(c) is also plotted in Fig. 6. According to Fig. 7, deviations between the results appear for $f_s > 200$ kHz. There, the minimum losses are nearly constant with respect to frequency if the Steinmetz parameters are adapted to the operating-point. A view on Fig. 6(a) reveals that the characteristic of α along the optimal trajectory experiences a sharp rise from 1.6 to 2.2 (approaching the value of β) around 200 kHz, and, at 300 kHz, enters the region where $\alpha \approx \beta$ applies. With this, Fig. 7 confirms the findings related to (14), (20), and (21), that the minimum losses, the optimal inductance, and the optimal number of turns are independent of frequency given that
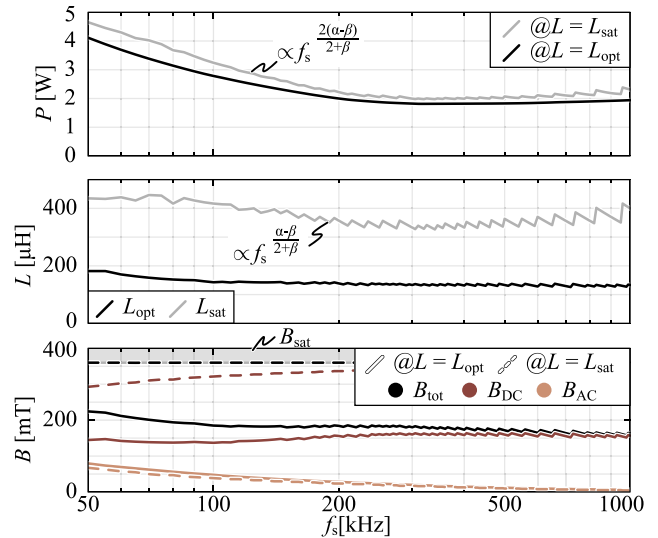
$\alpha = \beta$ applies. Moreover, the result confirms that the optimal designs are all limited by saturation.

D. STEINMETZ PARAMETERS DEPENDENT ON f_S, B_{AC}, B_{DC}

DC flux premagnetization has, potentially, a strong impact on the core losses of commonly employed magnetic core materials [30]. Fig. 3(d) depicts the contour plot of the core losses for DC premagnetization being considered. Compared to Fig. 3(c), an increase of the losses is observed in low-loss regions, e.g., at $f_s = 500$ kHz and $r = 10\%$. Furthermore, for given frequency, the minimum-loss trajectory, r_{opt}, yields a higher ripple than the trajectory r_{sat}. In order to investigate the reason for this result, Fig. 8 details the characteristics of losses, inductance, and flux densities along the two trajectories, which reveals a substantial decrease of B_{DC}, from approximately $300 - 350$ mT at $L = L_{sat}$ to 150 mT at $L = L_{opt}$. Furthermore, the losses increase only slightly when L increases from L_{opt} to L_{sat}, with a maximum deviation of 23.4% at 1 MHz and an average deviation of 12.6%. Accordingly, also the core losses and the total copper losses remain approximately similar, in order to maintain a loss ratio of 2 over β. Since the AC copper losses even increase for increasing ripple (the ratio $P_{Cu,AC}/P_{Cu,DC}$ reaches values between 20% and 30%, as shown with curve (iii) in Fig. 5), the loss reduction achieved by decreasing the inductance from L_{sat} to L_{opt} only stems from the reduction of the DC premagnetization, B_{DC}, that enables a reduction of the core losses.

E. MAIN OBSERVATIONS AND THE THREE QUASI-OPTIMAL RANGES

According to the above findings, optimal inductor designs feature a monotonically decreasing current ripple amplitude with increasing frequency that leads to an approximately constant inductance value. Moreover, designs with peak flux densities near saturation feature losses that are close to the optimum
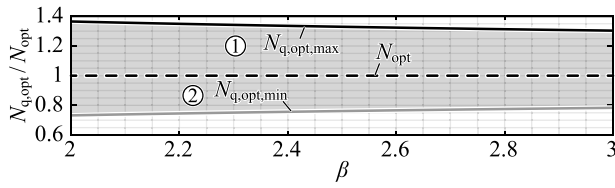
FIGURE 9. Relative deviation from the optimal number of turns as a function of β. The gray area denotes the range of N that leads to an increase of the total losses of less than 20%.

(for given frequency). The total losses decrease for increasing frequency, reaching a global loss minimum approximately at the point where the Steinmetz parameters α and β are equal. Around this point the total losses are relatively flat, with respect to all three design degrees of freedom: N, r, and f_s. In this regard, a range can be defined for each of the three degrees of freedom in order to identify inductor designs that feature almost minimum losses.

1) FLAT RANGE A – NUMBER OF TURNS

In case of flat range A, the ripple and the switching frequency are kept constant, and N is changed, starting from the optimal value, N_{opt}. The derivation starts with the total losses (6), which can be expressed as a function of the optimal number of turns (9), and while assuming already a loss ratio of 2 over β,

$$\frac{P_{tot}(N)}{P_{tot,opt}} = \frac{2}{2+\beta}\left[\frac{\beta}{2}\left(\frac{N}{N_{opt}}\right)^2 + \left(\frac{N}{N_{opt}}\right)^{-\beta}\right]. \quad (25)$$

Expression (25) enables the calculation of N for a defined acceptable increase of the total inductor losses (with respect to the minimum inductor losses). However, no closed form solution is found and (25) needs to be solved numerically, instead. Fig. 9 presents the boundaries of flat range A for an accepted loss increase of 20%, i.e., $P_{tot}(N)/P_{tot}(N_{opt}) = 1.2$, and $2 < \beta < 3$. The region enclosing the applicable range of N, $N_{q,opt,min} < N < N_{q,opt,max}$, is split into the two regions ① and ②. Region ① results in better performance at partial load and region ② results in better performance in case of overload operation. This will be further discussed in Section VI, where the design space diversity of the inductor is investigated. The depicted boundaries can be approximated by means of LMS fitting,

$$N_{q,opt,min} \approx (0.6343 + 0.0505\beta)N_{opt}, \quad (26)$$

$$N_{q,opt,max} \approx (1.4835 - 0.0610\beta)N_{opt} \quad (27)$$

(the error between numerical and approximated results is less than 0.2% for $2 < \beta < 3$). Please note that (26) and (27) are of universal character, i.e., not limited to the settings listed in Tables 1 and 2.

2) FLAT RANGE B – RIPPLE

This flat range considers changing ripple, constant frequency, and optimal number of turns (at each individual operating point); the corresponding trajectories are vertical lines in the

contour plots shown in Fig. 3. Fig. 4 illustrates respective examples for $f = 20$ kHz and $f = 375$ kHz and, in case of $f = 375$ kHz, reveals low total losses, close to the respective minima, within a relatively wide range of r. In addition, the impact of the DC bias on the core losses increases this range towards higher ripple values, due to the decreasing core losses, which provides a certain compensation of the increasing AC copper losses, cf. Section II-D.

3) FLAT RANGE C – ALONG L_{opt} TRAJECTORY

The last flat range is along the trajectory of optimal inductance, L_{opt}, highlighted in Fig. 3, and depends entirely on the relationship between α and β. For ferrite N87, this trajectory can be split into the two ranges listed below, cf. Fig. 8.

- 50 kHz $< f_s <$ 150 kHz: $\alpha \in [1.3, 1.6]$, $\beta \in [2.6, 2.7]$; with (14), $P_{tot,opt} \propto f_s^{-0.60} \ldots f_s^{-0.43} \approx 1/\sqrt{f_s}$ results;
- 250 kHz $< f_s <$ 850 kHz: $\alpha \approx \beta \approx 2$ applies, i.e., with (14), $P_{tot,opt}$ remains approximately constant.

The second range corresponds to flat range C and is an unchanged optimal design, since the inductance value and the number of turns remain approximately constant as well.

III. SEMI-NUMERICAL ANALYSIS

This Section revisits the analysis of Section II, using a detailed semi-numerical model in order to clarify that the drawn conclusions remain true if previously disregarded effects, in particular due to elevated temperatures of core and coil, are taken into consideration. For this, the analyzed range is slightly modified to the more practical range

$$40 \text{ kHz} \le f_s \le 1 \text{ MHz and } 2\% \le r \le 200\%. \quad (28)$$

The employed ElectroMagnetic-Thermal (EMT) coupled inductor model is entirely implemented in MATLAB [31] and provides the capabilities listed below.

- *Core losses* are calculated with the improved General Steinmetz Equation (iGSE) [32]. The Steinmetz parameters are extracted by means of interpolation, using pre-measured loss values, that take the implications of AC magnetic flux density, frequency, core temperature, and DC premagnetization into consideration [33]. The losses of the employed core material, N87, have been measured using the method proposed in [34].
- *AC copper losses* in the HF litz wire are determined according to [35] with the magnetic field in the core window being computed with the mirroring method [15].
- *The thermal model*, which is based on [28] and extended according to [33], considers the heat dissipation mechanisms of conduction, convection, and radiation in order to compute the surface temperatures of coil and core and the hot-spot temperature inside the coil.

The EMT model implements an iterative procedure to take the implications of elevated temperatures on core and copper losses into account, i.e., the losses and the temperatures are computed in a subsequent manner until both, losses and temperatures, reach convergence. The employed EMT modeling
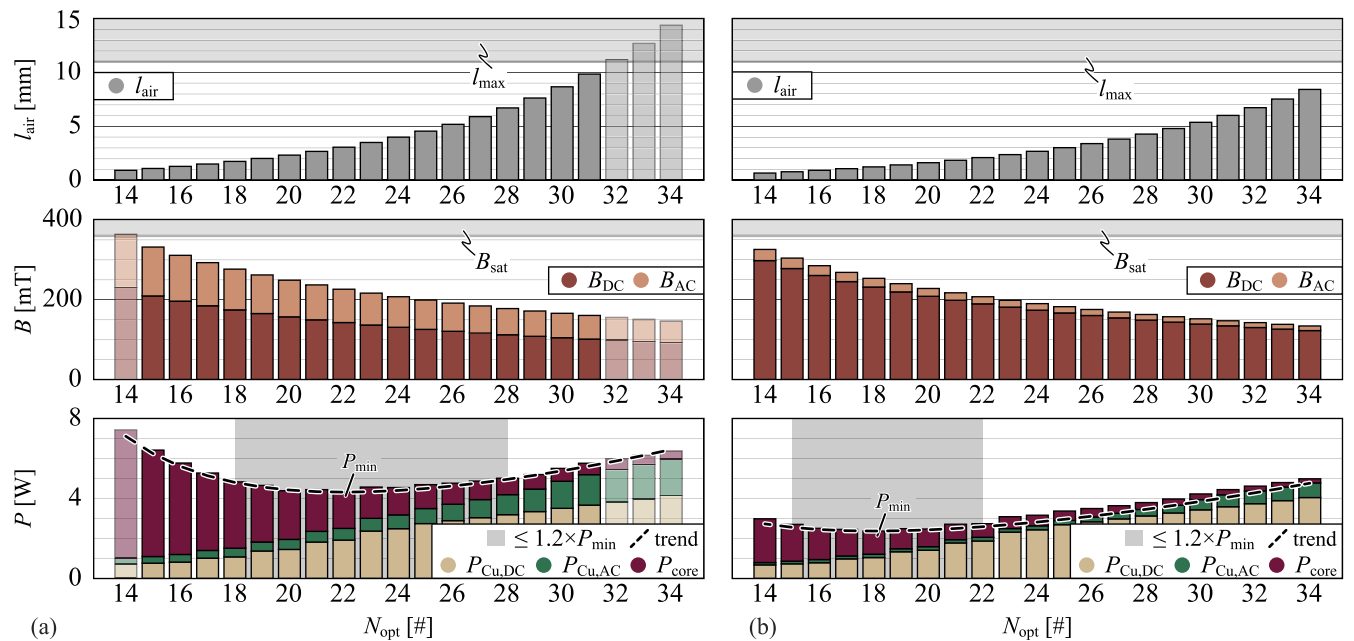
FIGURE 10. Air-gap length, flux density, and losses for different numbers of turns and two selected operating points: (a) $f_s = 80$ kHz, $r = 110\%$, (b) $f_s = 375$ kHz, $r = 18\%$. Local minima, P_{min}, and flat ranges A (cf. II-E1) are marked for both cases. The dashed trajectory denoted as trend corresponds to application of (25).

approach has been experimentally verified in several converter designs, e.g., [36], [37].

For the analysis, and unless otherwise specified, the following considerations apply:

1) The cooling of the component is entirely based on natural convection and no forced air-flow is considered.
2) The core has a single air gap per core limb (instead of the distributed air gap assumed in Section II to simplify the analysis), since this denotes a more common type of realization.

A. OPTIMIZATION WITH RESPECT TO N

For each operating point characterized with f_s and r, the number of turns is optimized with respect to the losses and, under the assumption of a constant fill factor, this is expected to lead to an approximately equal share between the core and copper losses. Fig. 10 reveals air-gap lengths, flux densities, and losses with respect to N for the two selected operating points $f_s = 80$ kHz, $r = 110\%$ and $f_s = 375$ kHz, $r = 18\%$ (the global loss minimum); these two operating points serve as basis for the further analysis and are referred to with OP$_1$ and OP$_2$, respectively.

The designs are limited by saturation in case of low N and by impractically large air gap values at high N, whereas the maximum air-gap lengths are limited to 30% of the height of the core window. Due to the varying fill factor, which results from the packaging of the turns, local optima exist.

Despite the varying fill factor, the applicability of (25) and (26), (27) is also confirmed by direct comparison with the peaks of the bars. Specifically, using i. for the case of 80 kHz

a β of 2.63,[8] N_{opt} equal to 22 and $P_{tot,opt}$ equal to 4.32 W, and ii. for the case of 375 kHz a β of 2.28,[9] N_{opt} equal to 18 and $P_{tot,opt}$ equal to 2.37 W the analytical solutions of flat range A are denoted as trend. The analytically derived margins of the quasi optimal operation using (26), (27) are [16.9, 29.1] and [13.5, 24.2] turns, respectively. Finally, the ratio between the core and copper losses varies around the theoretical $2/\beta$ from 0.2 to 2.2. Direct comparison between the two optimizations depicted in Fig. 10(a),(b) confirms the initial conclusion, that at higher frequency and lower ripple, the total losses decrease substantially.

B. OPTIMIZATION WITH RESPECT TO f_s AND r

Applying the presented local optimization with respect to the number of turns to all the points of (28), the contour plots of Fig. 11 result. Starting from Fig. 11(a) the total losses of each operating point of the optimization are presented. This contour is the equivalent of the analytically calculated result presented in Fig. 3(d). Even though, a direct comparison of the two contour plots reveals a similar trend with respect to loss-minimal operation, also significant deviations of the absolute losses can be observed. The main reasons for this difference are, the lower achieved fill factor, the more accurate estimation of the magnetic field inside the winding window, using the mirroring method, and the impact of the temperature on the core losses. Introduced noise, mainly apparent

---

[8]The value corresponds to a core temperature of 89° C AC magnetic flux density peak value of 80.2 mT and a DC premagnetization of 146 mT.

[9]The value corresponds to a core temperature of 77° C AC magnetic flux density peak value of 20.9 mT and a DC premagnetization of 233 mT.
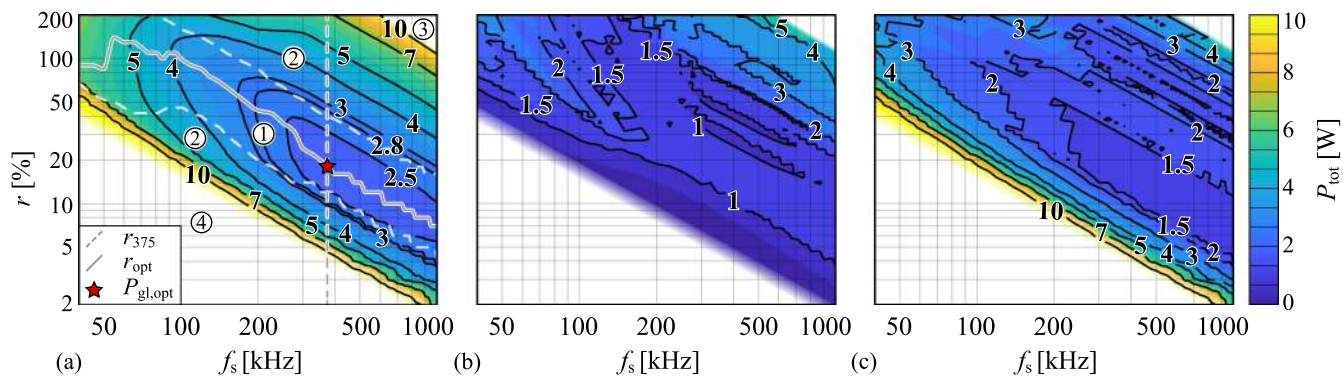
FIGURE 11. Contour plot of (a) total losses, (b) core losses, and (c) total copper losses, for the $f_s - r$-plane defined in (28). In (a), two trajectories are highlighted: r_{opt}, which corresponds to the minimum losses for changing frequency, and r_{375}, which corresponds to a changing ripple, a constant frequency of 375 kHz, and an optimum number of turns. The global optimum, $P_{gl,opt} = 2.4$ W, occurs at $f_s = 375$ kHz, $r = 18\%$ and is marked with a red star.

in Fig. 11(b), (c), results from the turn's packaging and the measured core loss data.

Fig. 11 also presents the global optimum, $P_{gl,opt} = 2.4$ W, which corresponds to OP$_2$, and two critical trajectories, i.e., the trajectory of minimum losses for changing frequencies, marked with r_{opt}, and the trajectory of changing ripple, constant frequency ($f = 375$ kHz), and optimal N, marked with r_{375}.

In the course of a closer inspection of Fig. 11(a), four characteristic regions are identified.

- Region ① is delimited by two dashed white lines, which illustrate the frequency-dependent changes of the two boundaries of the flat range B for a maximum increase of the losses by 20% [for a given frequency and with respect to the losses at $r_{opt}(f_s)$]. The designs within this region are most suitable for realization.
- Region ② corresponds to suboptimal designs, which are thermally valid, nevertheless, generate unnecessarily high losses.
- Regions ③ and ④ include invalid designs that will heat above the defined thermal limit, i.e., all temperatures must remain less than 125° C. Region ③ is limited by AC (copper and core) losses and region ④ by DC copper losses, cf. Figs. 11(b), (c).

Fig. 12 presents the contours of the corresponding hot-spot temperature inside the coil, T_{hs}, the peak magnetic flux density, and the optimal number of turns, respectively. The hot-spot temperature follows a trend that is identical to the trend of the total losses shown in Fig. 11(a) and remains less than 100 °C for $f > 100$ kHz and an assumed ambient temperature of 60 °C. According to Fig. 12(b), designs with peak flux densities ranging from 140 mT to 360 mT can result in optimal operation. This confirms the finding that, for increasing ripple, the decrease of the DC flux bias leads to a decrease of the core losses, which can compensate the increase of the AC copper losses within flat range B. Fig. 12(c) highlights the fact that with increasing frequency and/or ripple the optimal number of turns decreases in order to lower the impact of the AC copper losses on the total losses. In case of low ripple

values, the designs are limited by saturation, leading to a steep increase of the optimal number of turns for decreasing ripple. Finally, Fig. 12(c) also highlights the realized inductors and the operating points for experimental verification presented in Section VII.

C. INVESTIGATION OF r_{opt}

Fig. 13 presents the losses and the inductors' characteristic values (L, N, B, and J_{rms}) along the $r_{opt}(f_s)$ trajectory. The region of low losses, close to the global minimum of 2.4 W, is very flat and starts at 200 kHz. Based on this, operation above 200 kHz to 300 kHz may not provide us with additional benefits on a system level, since the remaining converter losses, e.g., switching losses of semiconductors, will keep increasing.

The graphs of L_{opt} and B in Fig. 13 confirm the finding of the analysis of Section II that, with respect to decreasing ripple, the flat range B extends to saturation limited designs. Fig. 14 presents a comparison of the optimal designs to the designs limited by saturation with respect to frequency and Fig. 15(a) depicts the corresponding Steinmetz parameters for the saturation limited designs, which confirm monotonically decreasing losses in case of $\alpha < \beta$ and constant losses for $\alpha \approx \beta$.

Close inspection of the flat region C at frequencies above the frequency featuring the global minimum reveals constant values of N_{opt}, L_{opt}, and AC copper losses and slowly increasing core losses. From (5), an increase of the core losses with increasing f_s is expected, since $\alpha > \beta$ applies in this region, cf. Fig. 15(a). With regard to the analysis of the AC copper losses, the factors F_r and G_r, used to compute the implications of skin and proximity effects in round wires [35], first need to be investigated. Fig. 16 depicts $F_r(f_s)$ and $G_r(f_s)$ and reveals that, for $d_r = 100$ μm, the losses due to skin effect, $P_{Cu,skin}$, are negligible in the considered frequency range ($F_r \approx 0.5$) and G_r is proportional to f_s^2. In addition, the AC magnetic field inside the winding window is proportional to $I_{AC,pk}$, which for constant L is inversely proportional to f_s, cf. (1). Based on the assumption that the proximity losses dominate the AC copper
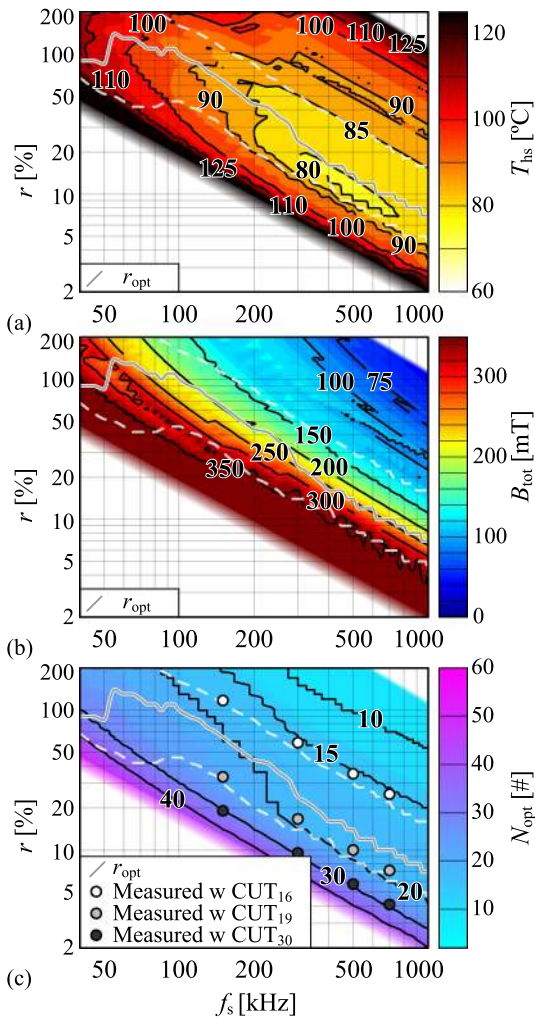
(a)

(b)

(c)

FIGURE 12. Contour plots of (a) hot-spot temperature inside the coil, (b) peak magnetic flux density, and (c) optimal number of turns. The presented values are used to compute the losses in Fig. 11.

losses (at 375 kHz the ratio between AC to DC resistance is equal to 20.4),

$$P_{Cu,AC} \approx R_{DC} \underbrace{G_r}_{\propto f^2} \underbrace{H_{AC,pk}^2}_{\propto f^{-2}} = \text{const.} \tag{29}$$

applies, which explains the constant AC copper losses at high frequencies observed in Fig. 13.

The ratio between the copper and core losses fluctuates around the theoretical optimal of $2/\beta$, for $f_s > 50$ kHz. This is attributed to small fluctuations of the fill factor and the integer number of turns. However, according to Fig. 13, $2/\beta$ does not apply for 40 kHz $< f_s < 50$ kHz and the optimal ratio of copper to core losses is found to be approximately $1/\beta$, instead. This result is linked to the copper fill factor, k_f, that results for technically possible arrangements of the conductors inside the core window for different values of N. Fig. 17 illustrates optimal fittings of litz wire with round cross section and for N ranging from 21 to 36 (due to half-plane symmetry only half of the E-core is shown and, in addition,
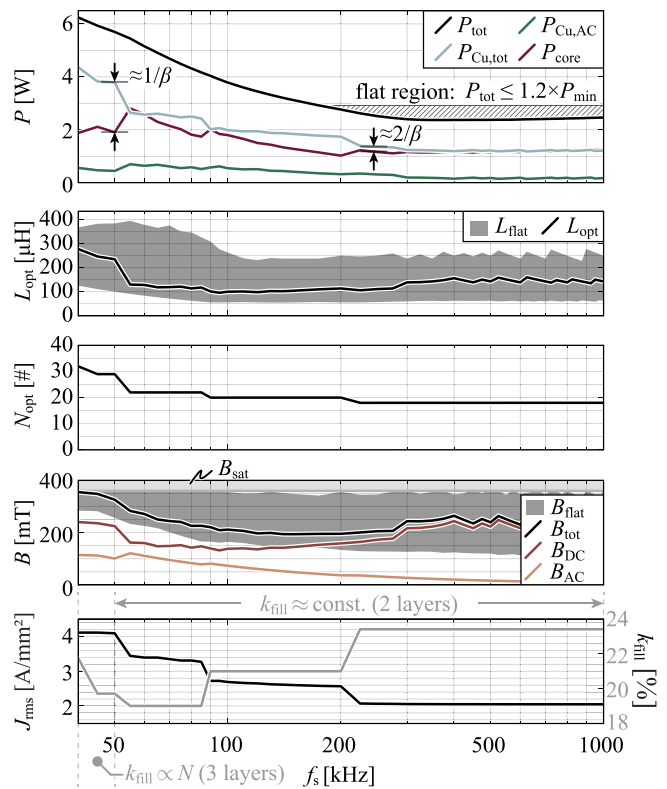

FIGURE 13. Losses and characteristic values of the corresponding inductor designs along the trajectory r_{opt} shown in Fig. 11(a). The result reveals the flat range C, which starts at 200 kHz. The gray regions shown in the graphs of L_{opt} and B denote suboptimal designs according to flat range B that feature an increase of the total losses by less than 20%.

the area occupied by the coilformer is highlighted). It can be observed that k_f ranges from 16.6% to 24.5%.

At higher frequencies, the optimal number of turns is close to 20 and the fill factor is approximately constant. However, at lower frequencies, N_{opt} increases and the inductor design enters the region of Fig. 17(c), where the wire diameter, d_{wire}, is constant (and comparably small, in order to accommodate three layers of conductors in the core window). Thus, k_f is proportional to N,

$$k_f = \frac{N A_{wire}}{A_w}, \tag{30}$$

where A_{wire} is the copper cross-section area of the conductor. With this,

$$R_{DC} = \frac{N l_{avg}}{\sigma k_f A_{wire}} \tag{31}$$

results, which gives total losses of

$$P_{tot} = c_7 N + c_2 N^{-\beta}, \tag{32}$$

$$c_7 = \frac{(32 f_s^2 I_{DC}^2 L^2 + c_0 V_o^2) l_{avg}}{32 \sigma A_{wire} f_s^2 L^2}, \tag{33}$$
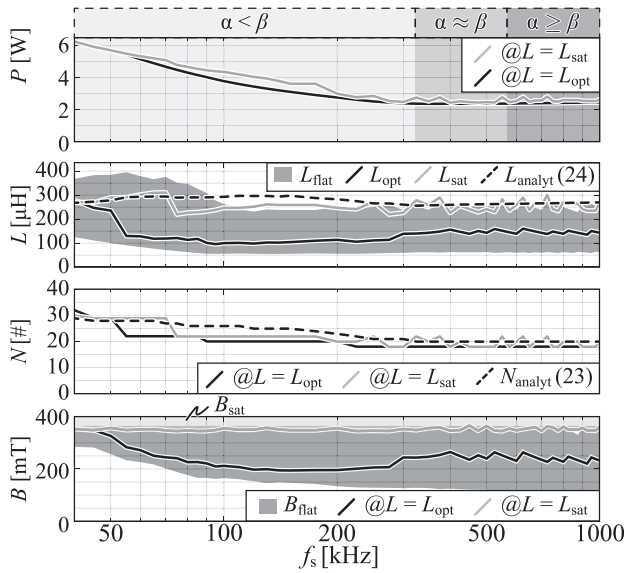
FIGURE 14. Comparison of the designs along the r_{opt} trajectory to the designs that are marginally limited by saturation in Fig. 11(a).
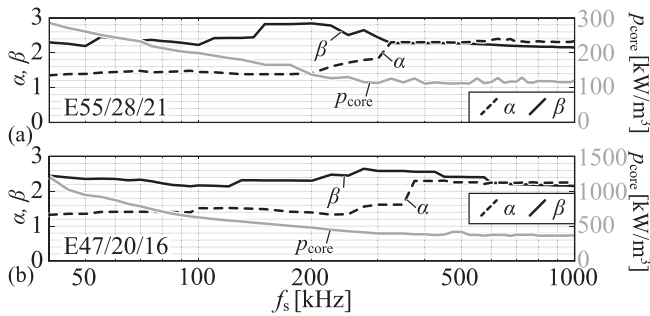

FIGURE 15. Steinmetz parameters α and β and core losses density, p_{core}, that correspond to the optimal designs along the r_{opt} trajectory of (a) the E55/28/21 core of Fig. 11(a) and (b) the E47/20/16 core of Fig. 19(c).

and, at the optimal number of turns, leads to a ratio of core to copper losses of

$$\left. \frac{P_{core}}{P_{Cu,tot}} \right|_{N=N_{opt}} = \frac{1}{\beta}. \tag{34}$$

D. TRAJECTORY OF CONSTANT FREQUENCY, r_{375}

Fig. 18 presents the losses and the inductor properties along the trajectory marked with r_{375} in Fig. 11(a), i.e., for a constant frequency of $f = 375$ kHz. Compared to the losses computed with the analytical model in Section II and presented in Fig. 4(b), substantial differences between the absolute values of the losses are observed that mainly arise from the operating-point dependent Steinmetz parameters. Yet, the trends and the absolute values of the ripple are almost identical and two main findings of the previous Section can be verified. Firstly, the total losses decrease for increasing L (decreasing r) and $L \leq L_{sat} \approx L_{opt}$. This is attributed to the AC copper losses, where the decrease of $I_{AC,pk}$ (and hence the $H_{AC,pk}$) dominates the minor increase of the optimal number of turns, i.e., N_{opt}, which remain constant for $18\% < r < 34\%$ and
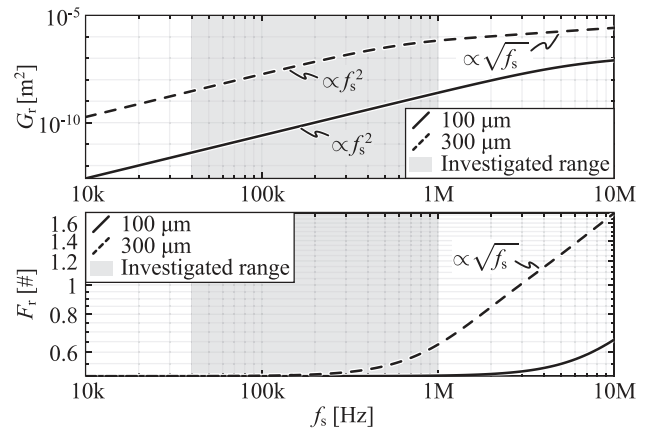

FIGURE 16. The factors for modeling AC losses due to proximity and skin effects, G_r and F_r, plotted against frequency and for two different single strand diameters of a litz wire, $d_r = 100$ μm and $d_r = 300$ μm.
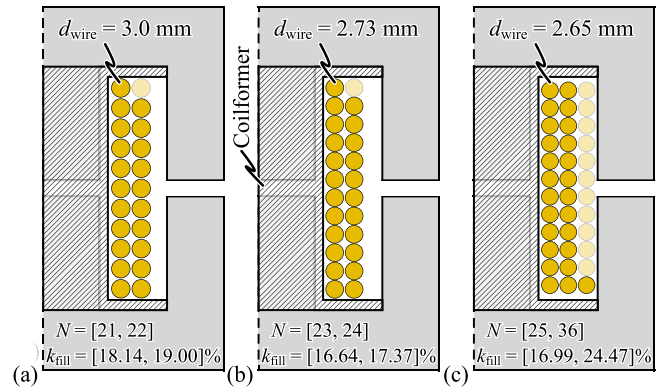

FIGURE 17. Turn packaging for an E55/28/21 core with coil former and round conductors, for $N \in [21, 36]$.

decrease only slightly for $34\% < r < 50\%$ (the value of G_r remains constant, due to consideration of constant frequency). Secondly, in accordance to the findings of Section II-E2, the value of B_{DC} increases for increasing L (decreasing r) and, with this, also the core losses slightly increase, which compensates the increase of the AC copper losses within flat range B, $11\% < r < 46\%$.

E. MAIN FINDINGS

With the proposed semi-numerical model, the main findings of Section II, namely optimal region of operation and main design trends, are confirmed, despite the different levels of detail of the employed models. The main difference lies in the absolute value of the total losses, which could lead to a thermally invalid design, if only the analytical approach is considered. In Section V, a direct comparison between the two models is conducted and the obtained result further confirms the above findings.

IV. VALIDATION WITH FURTHER DESIGNS

In order to confirm the generality of the above findings, three different cases, for same specifications of Table 1, are investigated with the EMT inductor model used in Section III:
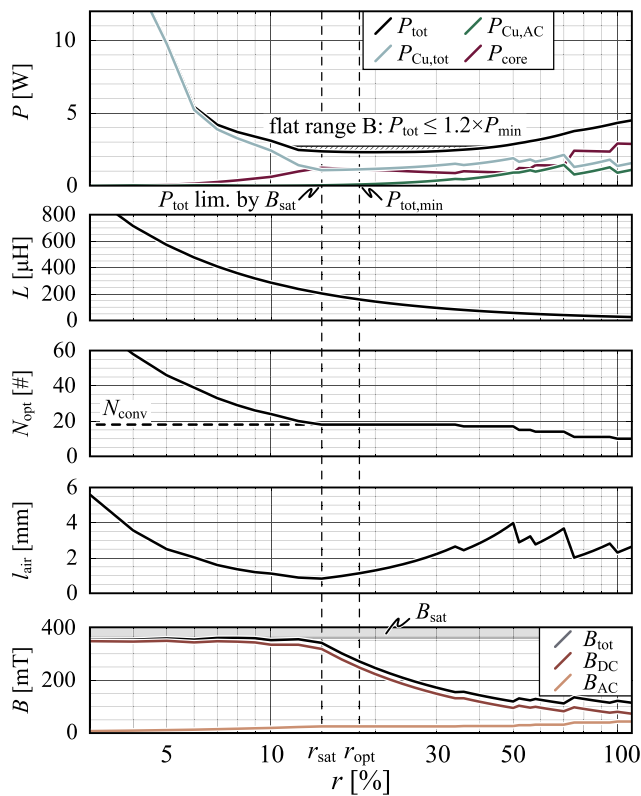
FIGURE 18. Detailed investigation of the losses and inductor properties determined with the EMT inductor model along the trajectory of varying ripple and constant frequency of $f_s = 375$ kHz, r_{375}, in Fig. 11(a). Flat range B, 11% < r < 46%, is highlighted.

1) Distributed air gap;
2) Litz wire strand diameter of 300 μm
3) Core E47/20/16 (smaller than E55/28/21).

A. DISTRIBUTED AIR GAP

For the analysis of the distributed air gap, seven symmetrically distributed air gaps at the center core-limb are considered. The contour plot of the total losses is depicted in Fig. 19(a). The basic observations are the following:

- The impact of the distributed air gap on the global loss minimum, the vicinity of the loss-optimal region, and the optimal frequency is relatively low; specifically, $P_{gl,opt}$ decreases from 2.4 W to 2.2 W and f_s changes from 375 kHz to 350 kHz.
- Compared to Fig. 11(a), the flat range B is wider, e.g., in comparison to the example analyzed in Section III-D, cf. Fig. 18, 10% < r < 64% applies at $f_s = 375$ kHz, which is due to reduced HF AC copper losses arising from the proximity effect. Accordingly, r_{opt} increases from 20% to 28% and the upper boundary of region ② of Fig. 11(a), i.e., a thermal limit of the inductor, is shifted towards higher ripple value.

On an inductor component level, the additional complexity resulting from the manufacturing of a core with distributed air gap is unfounded. Nevertheless, on a system level, increased ripple leads to less hard-switching semiconductor losses and,

thus, can be beneficial. However, this conclusion may not be valid in case of solid or foil conductors.

B. LITZ WIRE STRAND DIAMETER 300 μm

In case the litz wire strand diameter is increased, the absolute value of the losses increases. Interestingly, also the global optimum moves to higher frequencies (cf. Fig. 19(b)). This is mainly related to the value of G_r, depicted in Fig. 16. For a copper wire with a diameter of 300 μm and frequencies greater than 500 kHz, G_r is proportional to $\sqrt{f_s}$. As a result, (29) is not constant and the AC copper losses decrease for increasing frequency (the increase of F_r is of minor importance). Hence, the global optimum does not entirely depend on the core losses; in case of $d_r = 300$ μm, it is shifted to 1MHz, however, the minimum losses are found to be almost constant for 300 kHz < f_s < 1MHz (below 10% deviation). Finally, the upper boundary of region ② in Fig. 11(a) is shifted towards lower ripple values, due to poor HF performance and related thermal limitations.

C. CORE E47/20/16

The last case analyzed is the next smaller E-core of the series of TDK-EPCOS, E47/20/16, cf. Fig. 19(c). For this analysis, forced cooling of 4m/s air-speed is considered, since consideration of natural convection would significantly limit the valid operating area. With this air-speed and for given losses, the core temperatures are similar to the previously calculated temperatures for the E55/28/21 core.

Compared to Fig. 11(a), three characteristic differences are observed:

- Due to the smaller cross-sectional areas of core window and core, the current and flux densities increase, leading to increased losses, e.g., $P_{gl,opt}$ rises from 2.4 W to 3.51 W.
- The loss minimum is shifted towards higher ripple values, because the reduced volume leads to a decrease of the component's energy storage capability, rendering a lower inductance more suitable or, with regard to saturation, necessary.
- The optimal frequency is shifted to a higher value of 650 kHz. This is directly related to the increased optimal ripple, which leads to an increase of $B_{AC,pk}$ and, in turn, extends the frequency range where $\alpha < \beta$ applies towards higher frequencies, cf. Fig. 15(b).

V. FAST DESIGN GUIDE

According to Section III, the results of the detailed models confirm the results of the analytical model. The main difference are different absolute values of copper and core losses. Thus, a guide using analytical equations is proposed.

For a given frequency, the inductor is close to the optimal design for the following settings:

- L^* is chosen according to (21), in order to set the maximum magnetic flux density to the saturation magnetic
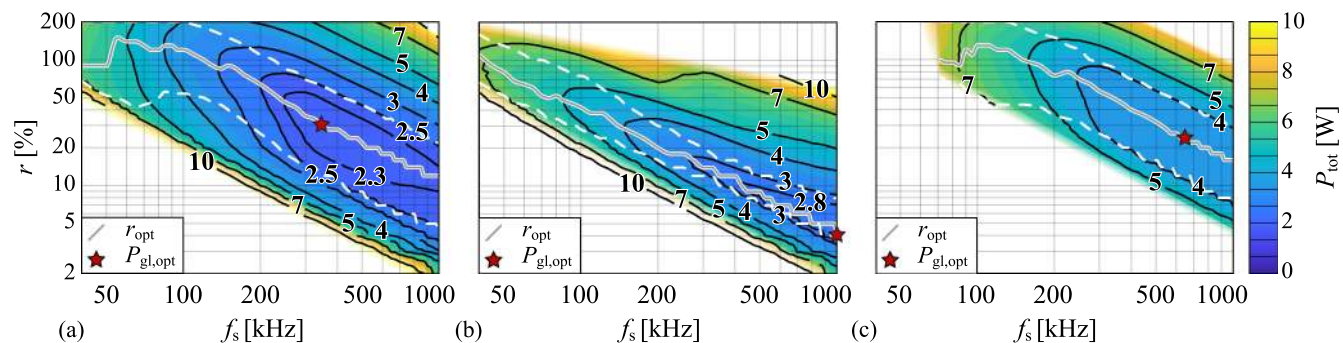
FIGURE 19. Contour plot of the total losses for three selected cases: (a) distributed air gap, (b) litz wire strand diameter of 300 μm, and (c) core E47/20/16. In each plot, the trajectory of $r_{opt}(f_s)$ and the global optima, $P_{gl,opt}$, are highlighted.
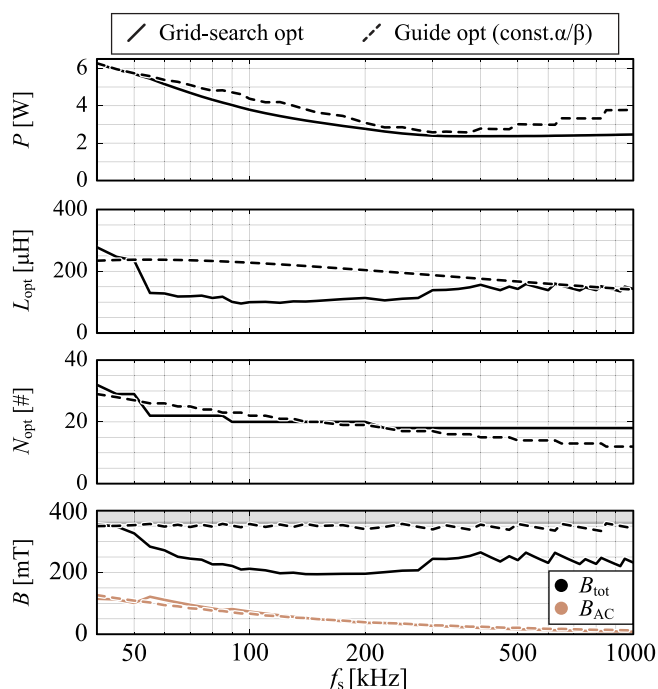

FIGURE 20. Comparison of losses and inductor properties for optimal designs, determined with a grid-search approach, and designs derived using the proposed "two-equation" guide. All designs are evaluated with the semi-numerical model.

flux density;

$$L^* = c_6 f_s^{\frac{\alpha-\beta}{2+\beta}} - \frac{V_o}{4 f_s I_{DC}}, \tag{35}$$

- N^* is chosen according to (9), in order to achieve a ratio of core to copper losses of $2/\beta$;

$$N^* = \left(\frac{\beta}{2}\frac{c_2}{c_1}\right)^{\frac{1}{2+\beta}}. \tag{36}$$

Fig. 20 presents a comparison of the designs obtained with this design guide, evaluated using the EMT inductor model, and the optimal designs that result from the EMT inductor model detailed in Fig. 13. Even though, the two approaches return different inductance values, similar losses result for

frequencies up to 500 kHz, which is related to the flat characteristic of the loss minimum. Between 40 kHz and 375 kHz, the maximum deviation between the two approaches is equal to 17.8% and occurs at 120 kHz.

If the operating frequency is not known in advance, the *PF* can be used to identify the optimal frequency range of the inductor with respect to minimum losses. The *PF* is defined for a given constant core loss density, $p_{core} = P_{core}/V_c$,

$$PF = B_{AC} f_s. \tag{37}$$

The consideration of the classical *PF*, instead of modified versions that consider HF AC losses, is based on the assumption that losses due to the proximity effect are low at the global optimum. Hence, the copper losses are constant with respect to frequency and the CUT performance depends entirely on the performance of the core.

In combination with (5),

$$B_{AC} = \frac{c_7}{f_s^{\frac{\alpha}{\beta}}}, \quad c_7 = \left(\frac{p_{core}}{k_{SE}}\right)^{\frac{1}{\beta}} \quad \Rightarrow \quad PF \propto f_s^{\frac{\beta-\alpha}{\beta}} \tag{38}$$

results, i.e., the *PF* increases for increasing frequency if $\alpha < \beta$ applies (and α is approximately constant). Furthermore, the *PF* peaks approximately at the frequency where α starts to rise significantly, which is close to the frequency where $\alpha = \beta$ applies. The *PF* data of N87 ferrite material for four different loss densities, ranging from 50 mW/cm³ to 300 mW/cm³, is depicted in Fig. 21. For $p_{core} = 50$ mW/cm³, the *PF* peaks at 285 kHz, which is close to optimal frequency calculated for in Section III for the inductor realized with the E55/28/21 core (there, $p_{core} \approx 30$ mW/cm³ applies), even though, the impact of the DC bias on the *PF* is not considered. For increased loss density, *PF* peaks at a higher frequency, which confirms the shift of $P_{gl,opt}$ of E47/20/16 to a higher frequency.

Please note that the proposed guide does not ensure thermal validity, which needs to be verified in a final step.

VI. DESIGN SPACE DIVERSITY

According to the results of the previous Sections, the total losses are close to the minimum within relatively wide ranges of N, r, and f_s, cf. Section II-E. In order to narrow the space
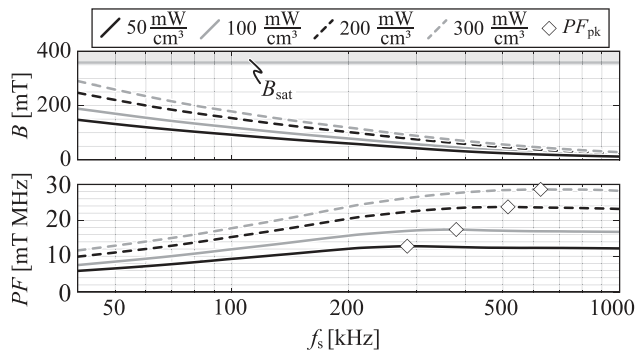
FIGURE 21. Performance Factor (*PF*) of N87 ferrite material for four different loss densities, i.e., 50 mW/cm³, 100 mW/cm³, 200 mW/cm³, 300 mW/cm³. The peak value of the *PF* for each value is highlighted.

of suitable designs, further criteria can be taken into account, e.g., partial-load efficiency and cost.

Fig. 22 depicts the design space diversity plot, i.e., the characteristic values of all possible designs, for the design settings of Table 2 and total losses of less than $1.2 \times P_{\text{opt,gl}}$, by taking all three design degrees of freedom into account (f_s, r, and N). Each y-axis represents the value of an individual variable and, depending on the background color, they are assigned to one of the three groups listed below.

1) Input design variables (light gray)
2) Internally computed variables (gray)
3) Main objectives (dark gray)

The newly defined main objectives are the relative component cost of the inductor, computed with respect to the minimum cost, and the inductor's efficiencies $\eta_{20\%}$, $\eta_{50\%}$, and $\eta_{100\%}$, which result if the buck converter is operated with an output power of 20%, 50%, and 100% of the rated power, respectively. The cost is calculated according to [38], which corresponds to a minimum order quantity of 15'000 pieces.

The result presented in Fig. 22 reveals that wide ranges of f_s, r, and N lead to almost minimum losses under full load conditions, however, with respect to cost and partial-load efficiencies, significant performance differences are observed. In order to further investigate this, the multi-objective optimization problem is solved in a grid-search approach by minimizing a cost function,

$$f_{\text{cost,obj},i} = w_1 \frac{P_{100\%,i}}{\max(P_{100\%})} + w_2 \frac{P_{50\%,i}}{\max(P_{50\%})} +$$
$$+ w_3 \frac{P_{20\%,i}}{\max(P_{20\%})} + w_4 \frac{cost_i}{\max(cost)},$$
$$\forall i \in \mathbb{N} \ \lor \ i \leq n, \quad (39)$$

where i refers to a dedicated design of the calculated design space (which itself comprises of n results),

$$w = [w_1, w_2, w_3, w_4] \quad (40)$$

denotes the user-defined optimization weights, and the four objectives are the total losses at full load ($P_{100\%,\text{norm}}$), 50%

load ($P_{50\%,\text{norm}}$) and 20% load ($P_{20\%,\text{norm}}$) and the cost per component.

Four different scenarios are investigated:

- *Scenario 1:* $w = [1.0, 0.0, 0.0, 0.0]$, i.e., minimum losses at full load.
- *Scenario 2:* $w = [0.247, 0.593, 0.16, 0.0]$; this is based on the weighted European efficiency for solar inverters [26],

$$\eta_{\text{Eu}} = 0.03\,\eta_{5\%} + 0.06\,\eta_{10\%} + 0.13\,\eta_{20\%}$$
$$+ 0.10\,\eta_{30\%} + 0.48\,\eta_{50\%} + 0.20\,\eta_{100\%}. \quad (41)$$

- *Scenario 3:* $w = [0.0, 0.2, 0.2, 0.6]$, i.e., low cost (higher priority) and low partial load losses (lower priority).
- *Scenario 4:* Worst case performance with respect to the additional main objectives (based on programmed logic script).

The *first scenario* shows that exclusive optimization for high efficiency at full load leads to missed opportunities, since both, partial load efficiency and cost, can be improved. Furthermore, with reference to the weights of (41), full load efficiency is of limited importance.

The *second scenario* follows the efficiency distribution of (41) and achieves a substantial improvement of the partial load efficiencies at the expense of a relatively low increase of the losses at full load, from 2.4 W to 2.72 W. This result is achieved with an increased number of turns and the design enters region ① in Fig. 9. Thus, the ratio of core to copper losses is less than $2/\beta$ for operation under full load. This ratio increases for decreasing output power, due to constant core losses and decreasing copper losses, which explains the improved partial-load efficiencies, cf. Section II-E1. Furthermore, a decreased cost results, which is unexpected, since scenario two does not take cost into consideration. This particular result is related to the fact that copper is an important cost driver and the coincidence that, in the presented case, the increased number of turns leads to a reduced fill factor and, thus, reduced copper mass. Due to this, a very similar result is obtained for the *third scenario*, i.e., increased number of turns, $N > N_{\text{opt}}$, to improve partial-load efficiency and decreased fill factor to lower the cost.

The *fourth scenario* demonstrates the missed opportunities of a bad design, even though, it features approximately similar frequency and losses as the design of scenario 2.

Based on the results of scenarios 2, 3 and in order to achieve improved partial-load efficiency and acceptable full-load efficiency, the design guide of Section V is used for the optimal frequency of 375 kHz and for the parameters of Table 2, nevertheless, this time N is optimized for a partial load of 50% using (9) (L is optimized for the nominal power using (21)). The resulting design, referred as Guide$_{50\%,\text{opt}}$, is depicted in Fig. 22.
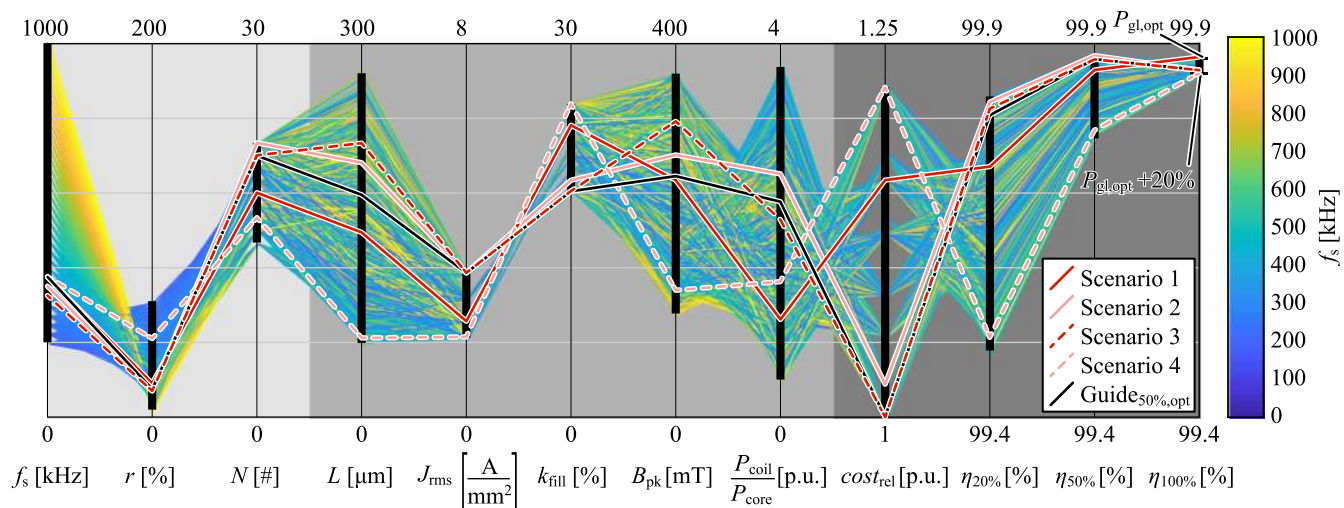
FIGURE 22. Design space diversity plot for the inductor, computed based on the settings summarized with Tables 1 and 2 and for maximum total losses of $1.2P_{gl,opt}$, cf. Fig. 11(a). The highlighted lines refer to: i. the four scenarios discussed in Section VI, ii. a quasi-optimal design at 375 kHz obtained using the proposed guide of Section V for L^* at full load and N^* at 50% partial load.
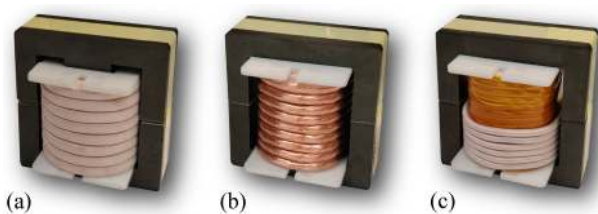

FIGURE 23. Constructed Devices Under Test (DUTs) for the verification of the findings of Section III. The DUTs employ an E55/28/21 core and litz wires with single-strand diameter of 100 μm. The number of turns and inductances of the DUTs are (a) $N = 16$, $L = 57$ μH, (b) $N = 19$, $L = 200$ μH, (c) $N = 30$, $L = 350$ μH.

VII. EXPERIMENTAL VERIFICATION

For the verification of the above-mentioned findings, three Devices Under Test (DUTs) are built, using the E55/28/21 N87 core and litz wire with a strand diameter of 100 μm, cf. Fig. 23. The components differ with regard to N and L:

- DUT_1: $N = 16$, $L = 57$ μH;
- DUT_2: $N = 19$, $L = 200$ μH;
- DUT_3: $N = 30$, $L = 350$ μH.

With this, the selected designs cover wide ranges of frequency (150 kHz to 700 kHz) [10] and ripple, cf. Fig. 12(c), to enable a thorough experimental verification of the discussed results. Specifically, DUT_1 and DUT_2 refer to designs with approximately optimal number of turns, however, in case of DUT_1 the AC copper losses and in case of DUT_2 the DC copper losses dominate the total copper losses. Finally, DUT_3 is a suboptimal design, limited by saturation, with dominating DC copper losses. According to the measured impedances of the DUTs, depicted in Fig. 24, and with a maximum test

---

[10]The value of 700 kHz is set as the maximum frequency, since no further improvements are expected above that frequency. Furthermore, the material approaches the maximum limit of its useful operating region (recommended maximum frequency according to [22] is 500 kHz).
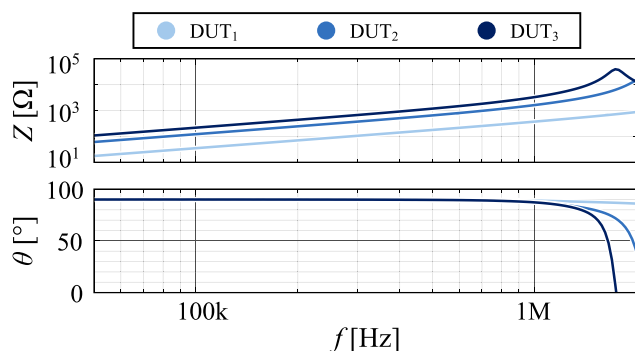

FIGURE 24. Measured phases and magnitudes of the impedances of the realized DUTs using a 4294 A impedance analyzer (by Agilent [39]). All three DUTs feature self-resonance frequencies well below the maximum operating frequency of 700 kHz.

frequency of 700 kHz, all three components are evaluated well below their self-resonance frequencies.

As opposed to the core losses, the measurement of the copper losses, in case of high frequency effects (i.e., proximity losses), is a challenging task, hence, the total losses of the designed DUTs are measured. Since the modeled core losses result from measured data, cf. Section III, the copper losses can be determined by subtracting the core losses from the total losses.

For the measurement of the total losses, a calorimetric setup, depicted in Fig. 25(a), is used [40], [41]. It consists of an inner calorimeter chamber and an outer reference chamber, which is used to ensure steady ambient conditions during the experiment. The calorimeter chamber accommodates the DUT and a heating device, i.e., a resistor, an attached heat sink, and fans, to ensure a homogeneous temperature inside the chamber. The employed setup enables measurements at a defined ambient temperature without the need
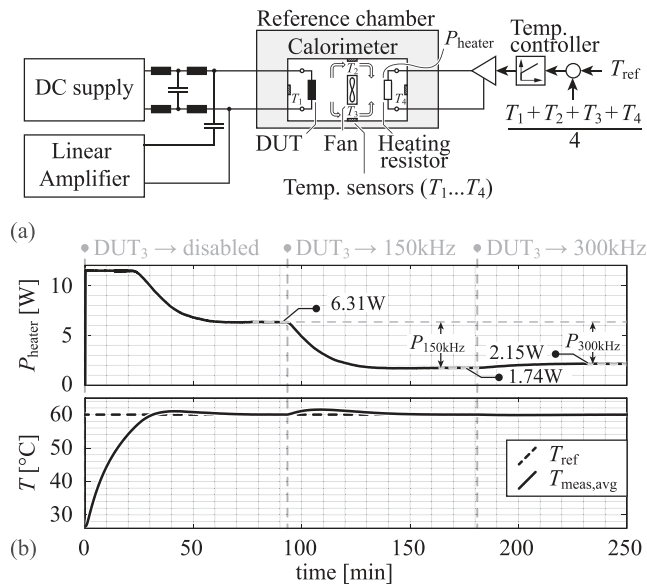
FIGURE 25. (a) Calorimeter setup used to measure the total losses generated by the Device Under Test (DUT) at the desired ambient temperature. (b) Losses of the heating device and temperature of the calorimeter chamber during the course of two consecutive experiments at 150 kHz and 300 kHz using DUT$_3$, cf. Fig. 23(c). The losses generated by the heating device during the three phases of steady-state are highlighted.
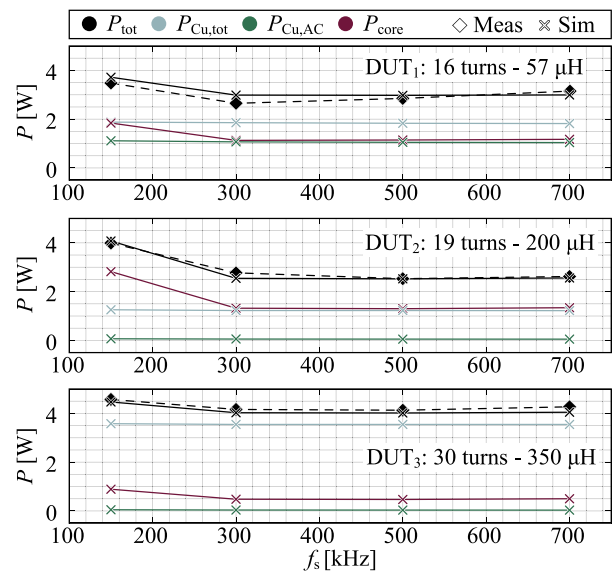

FIGURE 26. Comparison between the losses estimated using the EMT model (cf. Section III) and the losses using the calorimetric setup of Fig. 25(a), for the three DUTs of Fig. 23, at a reference (ambient) temperature of 60°C. The measurement of the two operating points at 150 kHz and 300 kHz of DUT$_3$ is shown in Fig. 25(b).

for pre-calibrations [40], [41]. The accuracy of the calorimeter has been assessed by means of reference loss measurements conducted with a 1kΩ power film resistor (RCH series by Vishay [42]), and two multimeters for measuring DC voltage and current (voltage: Fluke 233 [43], current: Fluke 175 [44]).[11] A consecutive measurement of four different losses, i.e., 2 W $\rightarrow$ 5 W $\rightarrow$ 2 W $\rightarrow$ 5 W, reveals maximum and average deviations of 54 mW and 35 mW, respectively, between the calorimetric and the electric measurement. For all four operating points, the resulting deviations, between the two measurement methods, lie within the uncertainty range of the employed multimeters.

For the excitation of the DUTs two sources are employed. The first source is a DC supply that provides the DC current, i.e., 10 A (cf. Table 1), and the second source is a linear amplifier that provides the AC voltage (up to 3 MHz). The two sources are connected in parallel and decoupled with two filters.

Fig. 25(b) presents the temperature inside the chamber during an experiment in order to illustrate the measurement procedure by way of example. Initially, the DUT is idle and the temperature-controlled heater increases the temperature inside the chamber to a defined value. After the system reaches steady state, the DUT is operated and the heater reduces its power to maintain a constant temperature. Once at steady state, the difference between the heating power before and after the excitation of the DUT corresponds to the losses of the DUT.

For the experimental verification of the findings of Sections II and III, the EMT model is exactly parameterized according to the corresponding DUT, e.g., the number of strands of the litz wire and the positions of the conductors (inside the core window and on the winding head). The measurements are conducted at a temperature of $T_{ref} = 60\,°C$. Fig. 26 presents the comparison of measured and calculated total losses for four different operating points per DUT. For the twelve measured operating points, the maximum deviation between calculated and measured results is 12.7% (for DUT$_1$ and $f_s = 300$ kHz) and the average absolute deviation is 4.85%, i.e., well below 20%, which is a commonly accepted uncertainty value for multi-domain component models. With this, the experimental results confirm the findings of this work.

VIII. CONCLUSION

In this work, the optimal operation of power inductors in common topologies, i.e., buck/boost switched converters, is analyzed. For the analysis and in order to achieve a comprehensible discussion of the various couplings and effects in inductors, the magnetic core (E55/28/21) and the employed litz wire (100 µm strand diameter) are fixed. The implications of the remaining design degrees of freedom, f_s, r, and N, are investigated with focus on the losses and optimal trends are identified. The analysis is done in two steps, initially with simplified analytical models and, subsequently, with a detailed semi-numerical multi-domain model. The link from the simplified to the detailed model is provided through a step-by-step introduction of different nonlinear effects (e.g., core saturation, impacts of frequency, AC magnetic flux density, and DC bias on the core losses). Experimental results confirm the theoretical findings. The experiments are conducted with

---

[11]During this measurement, DUT$_1$ was placed together with the resistor, in order to emulate the air-flow of the real experiments.

an accurate calorimetric method, three different inductors, and within a wide frequency range (150 kHz to 700 kHz).

Around the identified global loss optimum, a very flat characteristic of the losses is observed with respect to all three degrees of freedom. This property enables further potential opportunities with respect to reduced losses at partial load (e.g., 20% and 50% of rated load) and reduced cost, which come at the expense of an increase of the full-load losses by 15% to 20%. Furthermore, the obtained results enable the compilation of a simple two-equation guide to achieve designs that feature almost minimal losses for a given frequency. The total losses of the designs obtained using the proposed guide compared to the designs optimized using the detailed semi-numerical model feature a maximum deviation of 17.8% within a wide frequency range (40 kHz to 375 kHz).

REFERENCES

[1] J. W. Kolar, D. Bortis, and D. Neumayr, "The ideal switch is not enough," in *Proc. IEEE 28th Int. Symp. Power Semicond. Devices ICs.*, 2016, pp. 15–22.

[2] Z. Liu, F. C. Lee, Q. Li, and Y. Yang, "Design of GaN-based MHz totem-pole PFC rectifier," *IEEE Trans. Emerg. Sel. Topics Power Electron.*, vol. 4, no. 3, pp. 799–807, Sep. 2016.

[3] Z. Liu, B. Li, F. C. Lee, and Q. Li, "Design of CRM AC/DC converter for very high-frequency high-density WBG-based 6.6kW bidirectional on-board battery charger," in *Proc. IEEE Energy Convers. Congr. Expo. (ECCE USA)*, 2016, pp. 1–8.

[4] S. A. Mulder, "Fit formulae for power loss in ferrites and their use in transformer design," in *Proc. Int. Conf. Power Convers. Intell. Motion*, 1993, pp. 345–359.

[5] T. M. Undeland, J. Lode, R. Nilssen, W. P. Robbins, and N. Mohan, "A single-pass design method for high-frequency inductors," *IEEE Ind. Appl. Mag.*, vol. 2, no. 5, pp. 44–51, Sep.-Oct. 1996.

[6] M. Bogs and W. Holubarsch, "Design principles for high frequency power transformer materials," *Le J. de Physique IV*, vol. 7, no. C1, pp. 117–118, 1997.

[7] F. Forest, E. Laboure, T. Meynard, and M. Arab, "Analytic design method based on homothetic shape of magnetic cores for high-frequency transformers," *IEEE Trans. Power Electron.*, vol. 22, no. 5, pp. 2070–2080, Sep. 2007.

[8] A. J. Hanson, J. A. Belk, S. Lim, C. R. Sullivan, and D. J. Perreault, "Measurements and performance factor comparisons of magnetic materials at high frequency," *IEEE Trans. Power Electron.*, vol. 31, no. 11, pp. 7909–7924, Nov. 2016.

[9] M. Mogorovic and D. Dujic, "Sensitivity analysis of medium-frequency transformer designs for solid-state transformers," *IEEE Trans. Power Electron.*, vol. 34, no. 9, pp. 8356–8367, Sep. 2019.

[10] T. Guillod and J. W. Kolar, "Medium-frequency transformer scaling laws: derivation, verification, and critical analysis," *CPSS Trans.*, vol. 5, no. 1, pp. 18–34, 2020.

[11] J. Biela and J. W. Kolar, "Pareto-optimal design and performance mapping of telecom rectifier concepts," in *Proc. Int. Conf. Power Convers. Intell. Motion*, 2010, pp. 1–13.

[12] A. Stupar, T. Friedli, J. Miniböck, M. Schweizer, and J. W. Kolar, "Towards a 99 percent efficient three-phase buck-type PFC rectifier for 400 V DC distribution systems," in *Proc. IEEE Appl. Power Electron. Conf. Expo.*, 2011, pp. 505–512.

[13] Q. Li, M. A. E. Andersen, and O. C. Thomsen, "Research on power factor correction boost inductor design optimization — efficiency vs. power density," in *Proc. IEEE Energy Convers. Congr. Expo. (ECCE Asia)*, 2011, pp. 728–735.

[14] U. Badstuebner, A. Stupar, and J. W. Kolar, "Sensitivity of telecom dc-dc converter optimization to the level of detail of the system model," in *Proc. IEEE Appl. Power Electron. Conf. Expo.*, 2011, pp. 585–592.

[15] J. Muhlethaler, M. Schweizer, R. Blattmann, J. W. Kolar, and A. Ecklebe, "Optimal design of LCL harmonic filters for three-phase PFC rectifiers," *IEEE Trans. Power Electron.*, vol. 28, no. 7, pp. 3114–3125, Jul. 2013.

[16] A. Stupar, J. A. Taylor, and A. Prodic, "Posynomial models of inductors for optimization of power electronic systems by geometric programming," in *Proc. Workshop Control Model. Power Electron.*, 2016, pp. 1–8.

[17] K. Watanabe *et al.*, "Optimization of inductors using evolutionary algorithms and its experimental validation," *IEEE Trans. Magn.*, vol. 46, no. 8, pp. 3393–3396, Aug. 2010.

[18] T. Sato *et al.*, "3-D optimization of ferrite inductor considering hysteresis loss," *IEEE Tans. Magn.*, vol. 49, no. 5, pp. 2129–2132, May 2013.

[19] K. Booth and J. Bandler, "Space mapping for codesigned magnetics: Optimization techniques for high-fidelity multidomain design specifications," *IEEE Power Electron. Mag.*, vol. 7, no. 2, pp. 47–52, Jun. 2020.

[20] J. Leicht, A. Moses, and S. Zurek, "Hysteresis loss component under non-sinusoidal flux waveforms," in *proc. 18th Int. Symp. Soft Magn. Mater. J. Magnetism Magn. Mater.*, vol. 320, no. 20, 2008, pp. e608 – e610.

[21] T. Komma, "Allgemein gültiger Entwurfsalgorithmus für magnetische Komponenten in Schaltnetzteilen mit unterschiedlichen Topologien und Schaltfrequenzen bis 2 MHz," Ph.D. dissertation, Dresden Univ. Technol., 2004.

[22] "EPCOS Data Book 2013 - Ferrites and Accessories," Accessed: Sep. 1, 2020. [Online]. Available: https://www.tdk-electronics.tdk.com/download/519704/069c210d0363d7b4682 d9ff22c2ba503/ferrites-and-accessories-db-130501.pdf

[23] "Soft Ferrites and Accessories - Data Handbook 2013 - Ferroxcube," Accessed: Sep. 1, 2020. [Online]. Available: https://www.ferroxcube.com/en-global/download/download/11

[24] D. Bortis, D. Neumayr, and J. W. Kolar, "$\eta\rho$-Pareto optimization and comparative evaluation of inverter concepts considered for the GOOGLE Little Box Challenge," in *Proc. IEEE Workshop Control Model. Power Electron.*, 2016, pp. 1–5.

[25] M. Leibl, "Three-phase PFC rectifier and high-voltage generator for X-ray systems," Ph.D. dissertation, Dep. Info. Technol. Elect. Eng. (D-ITET), Power Electro. Sys. Lab. (PES), ETH Zurich, Switzerland, 2017.

[26] R. Hotopp, "Private photovoltaic power generation systems in parallel grid operation: Planning, installation, operation, profitability." Expert advice on renewable energies (in German). RWE Energie, 1991.

[27] E. C. Snelling, *Soft Ferrites, Properties Applications*. London, U.K.: Butterworths, 2nd edition, 1988.

[28] V. C. Valchev and A. Van den Bossche, *Inductors Transformers Power Electron*. Boca Raton, FL, USA: CRC Press, 2005.

[29] W. G. Hurley and W. H. Wölfle, *Transformers Inductors Power Electron.: Theory, Des. Appl.* Hoboken, NJ, USA: John Wiley & Sons, Inc., Wiley, 2013.

[30] J. Muhlethaler, J. Biela, J. W. Kolar, and A. Ecklebe, "Core losses under the DC bias condition based on Steinmetz parameters," *IEEE Trans. Power Electron.*, vol. 27, no. 2, pp. 953–963, Feb. 2012.

[31] "MATLAB v. 9.5," (MathWorks Inc, Natick Massachusetts, United States). [Online]. Available: https://www.mathworks.com

[32] Jieli Li, T. Abdallah, and C. R. Sullivan, "Improved calculation of core loss with nonsinusoidal waveforms," in *Proc. IEEE Ind. Appl. Conf.*, vol. 4, 2001, pp. 2203–2210.

[33] R. Burkart, "Advanced modeling and multi-objective optimization of power electronic converter systems," Ph.D. dissertation, ETH Zurich, Switzerland, 2016.

[34] M. Mu, Q. Li, D. J. Gilham, F. C. Lee, and K. D. T. Ngo, "New core loss measurement method for high-frequency magnetic materials," *IEEE Trans. Power Electron.*, vol. 29, no. 8, pp. 4374–4381, Aug. 2014.

[35] J. Ferreira, "Analytical computation of AC resistance of round and rectangular litz wire windings," *IEE Proc. B – Electric Power Appl.*, vol. 139, no. 1, p. 21–25, Jan. 1992.

[36] M. Antivachis, D. Wu, D. Bortis, and J. W. Kolar, "Analysis of double-bridge inverters for drive systems with open-end winding motors," *IEEE Trans. Emerg. Sel. Topics Power Electron. - Early Access*, 2020.

[37] M. Antivachis, J. A. Anderson, D. Bortis, and J. W. Kolar, "Analysis of a synergetically controlled two-stage three-phase DC/AC buck-boost converter," *IEEE CPSS Trans. Power Electron. Appl.*, vol. 5, no. 1, pp. 34–53, Mar. 2020.

[38] R. Burkart and J. W. Kolar, "Component cost models for multi-objective optimizations of switched-mode power converters," in *Proc. IEEE Energy Convers. Congr. Expo. (ECCE USA)*, 2013, pp. 2139–2146.

[39] "Agilent 4294A - Precision Impedance Analyzer 40 Hz to 110 MHz," Accessed: Jun. 17, 2020). [Online]. Available: http://literature.cdn.keysight.com/litweb/pdf/5968-3808E.pdf

[40] T. Kleeb, B. Dombert, S. Araújo, and P. Zacharias, "Loss measurement of magnetic components under real application conditions," in *Proc. Eur. Conf. Power Electron. Appl.*, pp. 1–10, 2013.

[41] P. Papamanolis, F. Krismer, and J. W. Kolar, "Minimum loss operation of high-frequency inductors," in *Proc. IEEE Appl. Power Electron. Conf. Expo.*, 2018, pp. 1756–1763.

[42] "Power Resistor, for mounting onto a heatshink thick film technology," Accessed: Jun. 14, 2020. [Online]. Available: https://www.vishay.com/docs/50006/rch.pdf

[43] "Fluke 233 remote display digital multimeter," Accessed: Jun. 14, 2020. [Online]. Available: https://www.fluke.com/en/product/electrical-testing/digital-multimeters /fluke-233

[44] "Fluke 175 true-RMS digital multimeter," Accessed: Jun. 14, 2020. [Online]. Available: https://www.fluke.com/en/product/electrical-testing/digital-multimeters /fluke-175

[45] M. S. Rylko, B. J. Lyons, J. G. Hayes, and M. G. Egan, "Revised magnetics performance factors and experimental comparison of high-flux materials for high-current DC–DC inductors," *IEEE Trans. Power Electron.*, vol. 26, no. 8, pp. 2112–2126, Aug. 2011.

[46] W.-J. Gu and R. Liu, "A study of volume and weight vs. frequency for high-frequency transformers," in *Proc. 24th IEEE Power Electron. Specialists Conf.*, 1993, pp. 1123–1129.

[47] "Ferrite magnetic design tool," Accessed: Jan. 13, 2020. [Online]. Available: https://www.tdk-electronics.tdk.com/en/180490/design-support/design-too ls/ferrite-magnetic-design-tool

[48] P. Papamanolis, T. Guillod, F. Krismer, and J. W. Kolar, "Transient calorimetric measurement of ferrite core losses up to 50MHz," *IEEE Trans. Power Electron. - Early Access*, 2020.

[49] J. Muhlethaler, J. W. Kolar, and A. Ecklebe, "A novel approach for 3D air gap reluctance calculations," in *Proc. 8th Int. Conf. Power Electron.*, 2011, pp. 446–452.

[50] J. W. Kolar, F. Krismer, Y. Lobsiger, J. Muhlethaler, T. Nussbaumer, and J. Minibock, "Extreme efficiency power electronics," in *Proc. Int. Conf. Integr. Power Electron. Syst.*, 2012, pp. 1–22.

FLORIAN KRISMER (Member, IEEE) received the Dipl.-Ing. (M.Sc.) degree in electrical engineering with specialization in automation and control technology from the Vienna University of Technology, Vienna, Austria, in 2004, and the Ph.D. degree in electrical engineering from the Department of Information Technology and Electrical Engineering, ETH Zurich, Zurich, Switzerland, in 2010. He is currently a Research Associate with Power Electronic Systems Laboratory (PES), ETH Zurich, where he has cosupervised Ph.D. students and has continued with his research in the field of power electronics. He is the author or coauthor of numerous conference and peer-review publications. Dr. Krismer is the recipient of two awards for his publications. His research interests include the analysis, design, and general optimization of power converter systems, e.g., the weight optimization of a bidirectional dc–dc converter for an airborne wind turbine. Furthermore, he conducts research related to the filtering of conducted electromagnetic emissions and collaborated in the littlebox-challenge with respect to the hardware realization.

PANTELEIMON PAPAMANOLIS (Student Member, IEEE) studied electrical engineering at the National Technical University of Athens (NTUA), Athens, Greece, with majors in energy conversion and electric power systems. In 2014, he continued his M.Sc. studies at ETH Zrich in robotics, systems and control. Since 2016, he is working toward the Ph.D. degree at Power Electronic Systems Laboratory, ETH Zurich, Zurich, Switzerland, focusing on the modeling, optimization, and measurement of magnetic components and on three-phase ac/dc rectifier converters for EV charging applications.

THOMAS GUILLOD (Member, IEEE) received the M.Sc. degree in electrical engineering and information technology from ETH Zurich, Zurich, Switzerland, in 2013, with a focus on power electronics, numerical analysis, and field theory. In 2013, he joined the Power Electronic Systems Laboratory, ETH Zurich, as a Ph.D. Student and, in 2018, as a Postdoctoral Researcher. His current research interests include medium-voltage converters, high-frequency magnetic components, design and optimization methods, and numerical modeling methods.

JOHANN W. KOLAR (Fellow, IEEE) received the M.Sc. degree in industrial electronics and control engineering and the Ph.D. degree in electrical engineering (*summa cum laude/promotio sub auspiciis praesidentis rei publicae*) from the Vienna University of Technology, Vienna, Austria, in 1997 and 1999, respectively. Since 1984, he has been working as Independent Researcher and International Consultant in close collaboration with the Vienna University of Technology, in the fields of power electronics, industrial electronics, and high performance drive systems. He is currently a Full Professor and the Head of the Power Electronic Systems Laboratory, Swiss Federal Institute of Technology (ETH) Zurich, Switzerland. He has proposed numerous novel pulsewidth modulation converter topologies, modulation and control concepts, multiobjective power electronics design procedures, etc. and has supervised 70+ Ph.D. students. He has authored or coauthored 900+ scientific papers in international journals and conference proceedings, four book chapters, and has filed 190+ patents. He has presented 30+ educational seminars at leading international conferences and has served as IEEE PELS Distinguished Lecturer from 2012 through 2016. Dr. Kolar is the recipient of 36 IEEE Transactions and Conference Prize Paper Awards, the 2014 IEEE Power Electronics Society R. David Middlebrook Achievement Award, the 2016 IEEE William E. Newell Power Electronics Award, the 2016 IEEE PEMC Council Award, and two ETH Zurich Golden Owl Awards for excellence in teaching. He has initiated and/or is the Founder of four ETH Spin-off companies. The focus of his current research is on ultra-compact and ultra-efficient SiC and GaN converter systems, ANN-based power electronics components and systems design, solid-state transformers, power supplies on chip, as well as ultra-high speed and ultra-light weight drives, bearingless motors, and energy harvesting.